CANCER

MYO10 drives genomic instability and inflammation in cancer

Franklin Mayca Pozo[1], Xinran Geng[1], Ilaria Tamagno[2], Mark W. Jackson[2], Ernest G. Heimsath[3], John A. Hammer[4], Richard E. Cheney[3], Youwei Zhang[1]*

Genomic instability is a hallmark of human cancer; yet the underlying mechanisms remain poorly understood. Here, we report that the cytoplasmic unconventional Myosin X (MYO10) regulates genome stability, through which it mediates inflammation in cancer. MYO10 is an unstable protein that undergoes ubiquitin-conjugating enzyme H7 (UbcH7)/β-transducin repeat containing protein 1 (β-TrCP1)–dependent degradation. MYO10 is upregulated in both human and mouse tumors and its expression level predisposes tumor progression and response to immune therapy. Overexpressing MYO10 increased genomic instability, elevated the cyclic GMP-AMP synthase (cGAS)/stimulator of interferon genes (STING)–dependent inflammatory response, and accelerated tumor growth in mice. Conversely, depletion of MYO10 ameliorated genomic instability and reduced the inflammation signaling. Further, inhibiting inflammation or disrupting *Myo10* significantly suppressed the growth of both human and mouse breast tumors in mice. Our data suggest that MYO10 promotes tumor progression through inducing genomic instability, which, in turn, creates an immunogenic environment for immune checkpoint blockades.

INTRODUCTION

Genomic instability often refers to the existence of a variety of DNA alterations, ranging from single nucleotide changes (such as base substitution, deletion, and insertion) to chromosomal rearrangements (e.g., gain or loss of a segment or the whole chromosome) (*1*). Loss of genome stability can lead to early onset or accelerate the progression of degenerative diseases including premature aging and cancer. Genomic instability is a hallmark of most human cancers and generally correlates with cancer patient prognosis and therapy selection (*2*, *3*). However, our understanding about how genomic instability is regulated and how it promotes tumor development remains incomplete.

Because of the location of DNA/chromosomes in the nucleus, genomic instability has been conventionally considered to be a pathophysiological event that takes place in the nucleus, where DNA sequence, chromosome number, and/or structures are altered by endogenous or exogenous stimuli. For instance, carcinogens or irradiation can directly damage DNA; mutations in genes controlling DNA replication, repair, or chromosomal segregation cause DNA/chromosomal instability; and defects in the nuclear structure alter chromosome territory and impair chromosomal metabolism (*4*). Recent evidence suggests that the cytosol-nucleus connection network, or the so-called linker of nucleoskeleton and cytoskeleton (LINC) complex, also affects genome stability (*5*). The LINC complex contains sad1 unc-84 domain protein 1 (SUN) proteins that span the inner nuclear membrane and connect to the nuclear lamina and Nesprin proteins that are tail-anchored to the outer nuclear membrane and connect to SUN proteins in the lumenal region of the nuclear envelope (*6*–*8*). The cytoskeletal networks to which the LINC complex connects through Nesprin proteins include microtubules, intermediate filaments, and actin fibers (*8*). Mutation in genes involved in the LINC complex or the nuclear envelope has been shown to result in abnormal nuclear morphology, transcriptional deregulation, and DNA repair defect, highlighting the importance of a delicate cytoskeleton-nucleus connection in maintaining genome stability (*6*–*11*).

Genomic instability caused by nuclear envelope ruptures or mitotic drug treatment has the potential to trigger the cyclic GMP-AMP synthase (cGAS)/stimulator of interferon genes (STING)–mediated inflammatory response as a result of the recognition of cytosolic DNA, particularly micronuclei (*12*, *13*). However, genomic and micronuclei DNA triggered weaker cGAS/STING response than viral DNA (*13*, *14*), likely because they contain nucleosome structures that prevented cGAS from being activated (*15*). Additional mechanisms are also crafted to limit activation of the cGAS/STING pathway toward genomic or micronuclei DNA, such as the competition between cGAS and barrier-to-autointegration factor (BAF) for binding to genomic DNA (*16*) and sequestration of the nuclease three-prime repair exonuclease 1 (TREX1) in the endoplasmic reticulum (*17*). Nevertheless, continuous activation of the cGAS/STING pathway driven by genomic instability has been reported to induce chronic inflammation, fueling cancer progression probably by suppressing cytotoxic T cells in the tumor microenvironment (*12*, *18*).

The myosin family contains diverse actin-binding motor proteins (*19*). While conventional type II myosin proteins regulate skeletal muscle contraction and cell migration, most of the remaining unconventional myosins function in cellular processes such as intracellular transport and tethering, cell division, cell motility, cytoskeleton organization, etc. (*20*). Myosin X (MYO10) (not MYH10) is an unconventional myosin that binds to actin filaments (*21*). It is also known to localize to the tips of filopodia (*22*, *23*), finger-like membrane protrusions that are often associated with cellular movement (*24*, *25*). Hence, MYO10 has been indicated to regulate cell adhesion, spindle orientation, cell-cell junction, and cell motility and is involved in wound healing, tumor invasion, neuronal extension, etc. (*20*, *23*).

MYO10 was shown to be up-regulated in a wide range of human cancers including melanoma, breast cancer (*26*), leukemia (*27*), and lung cancer (*28*). High expression levels of MYO10 correlated with

[1]Department of Pharmacology, Case Comprehensive Cancer Center, Case Western Reserve University School of Medicine, Cleveland, OH 44106, USA. [2]Department of Pathology, Case Comprehensive Cancer Center, Case Western Reserve University School of Medicine, Cleveland, OH 44106, USA. [3]Department of Cell Biology and Physiology, School of Medicine, University of North Carolina at Chapel Hill, Chapel Hill, NC 27599, USA. [4]Cell and Developmental Biology Center, National Heart, Lung and Blood Institute, Bethesda, MD 20892, USA.
*Corresponding author. Email: yxz169@case.edu

breast and skin cancer aggressiveness and indicated poorer patient survival (*26*, *29*). MYO10 up-regulation seems to be important for metastasis of *TP53* mutant breast cancer (*30*). These findings suggest a potentially important role of MYO10 in cancer development. However, how MYO10 is regulated and how its up-regulation promotes cancer progression are poorly understood. Here, we report a previously uncharacterized role of MYO10 in maintaining nuclear structural integrity and genome stability. We show that the protein level of MYO10 is critical for this function and reveal that MYO10 undergoes ubiquitination and proteasomal degradation by ubiquitin-conjugating enzyme H7 (UbcH7) and β-transducin repeat containing protein 1 (β-TrCP1). We further demonstrate that MYO10 regulates the cGAS/STING-dependent inflammatory response and affects cancer progression and response to immune checkpoint blockades (ICBs).

RESULTS

Loss of UbcH7 leads to abnormal nuclear morphology

We previously reported that UbcH7 (encoded by *UBE2L3*), a ubiquitously expressed E2 enzyme (*31*), mediates DNA damage repair by regulating the protein level of an important DNA damage response factor 53BP1 (*32*, *33*). During analysis to further understand the biological function of UbcH7, we unexpectedly found that A549 lung cancer cells stably depleted of UbcH7 (fig. S1A) exhibited a significantly elevated rate of abnormal nuclear structures (including nuclear envelope bleb, rupture, protrusion, and breakage) when stained with the anti–lamin A/C antibody (Fig. 1, A and B). Conversely, the cellular circularity was significantly reduced by UbcH7 depletion (Fig. 1C). The antibody specificity was confirmed by RNA interference (RNAi)–mediated depletion of cognate genes (Fig. 1A and fig. S1, A and B). UbcH7 depletion only moderately increased the percentage of S phase cells (*32*, *34*). Given that nuclear envelope breakdown occurs in mitosis, these abnormal nuclear structures were unlikely caused by the minor S phase accumulation in the absence of UbcH7. In contrast, depletion of cathepsin L (CTSL), a lysosomal cysteine proteinase that shows similar cellular localization as UbcH7 (fig. S1C), did not alter the nuclear morphology (Fig. 1, B and C, and fig. S1C), suggesting that the increased nuclear structural abnormalities are specific to UbcH7 depletion.

Abnormal nuclear structures were also confirmed by examining the localization of lamin B1 (Fig. 1, D to F), another component of the nuclear envelope. We observed the same abnormal nuclear morphology in UbcH7 stably depleted HeLa cells (fig. S1, D to F), UbcH7–transiently depleted A549 cells (fig. S1, G to I), and in UbcH7 stably depleted nontransformed human fibroblast IMR-90 cells (fig. S2, A to D). Stably reintroducing RNAi-resistant Flag-tagged UbcH7 wild type (WT) into UbcH7-depleted A549 cells (Fig. 1G) completely reverted the elevated nuclear structural abnormalities in these cells (Fig. 1, H to J), confirming that the nuclear structural abnormalities were directly caused by UbcH7 depletion.

MYO10 is a critical substrate for UbcH7 in regulating the nuclear structural integrity

An important question then is how UbcH7 mediates the nuclear structure integrity. Immunostaining did not reveal an accumulation of UbcH7 around the nuclear envelope region (Fig. 1A), suggesting

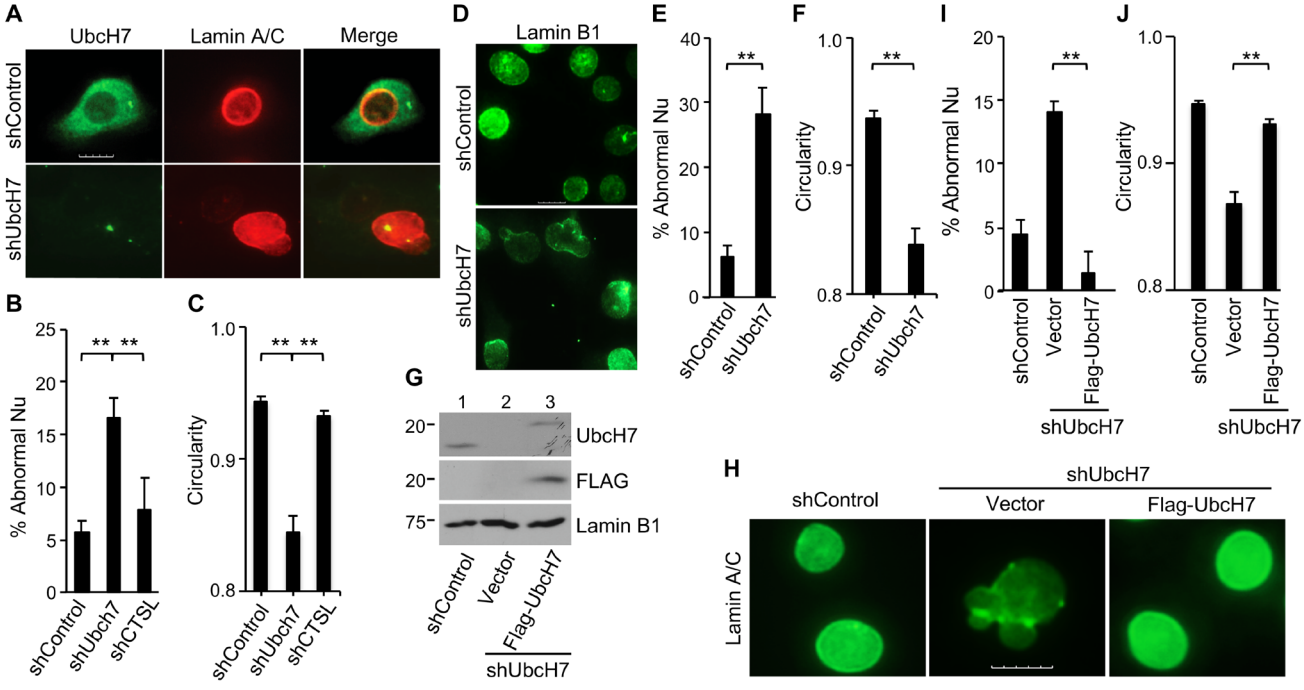

Fig. 1. UbcH7 regulates the nuclear morphology. (**A**) A549 control or UbcH7 stably depleted cells were immunostained with anti-UbcH7 and anti–lamin A/C antibodies. Representative images are shown. (**B**) Percentage of cells from (A) and fig. S1C with abnormal nucleus (Nu) including blebs, ruptures, protrusions, etc., were counted. Scoring was not blind. (**C**) Circularity of the nucleus from cells in (A) and fig. S1C. (**D**) A549 control or UbcH7 stably depleted cells were immunostained with anti–lamin B1 antibodies. Representative images are shown. Quantitative results of abnormal nuclear structures (**E**) or the nucleus circularity (**F**) from cells in (D). (**G**) UbcH7-depleted A549 cells were stably transfected with vector control or RNAi-resistant FLAG-UbcH7, and protein expression was examined by Western blot. (**H**) Representative images of the nuclear morphology visualized by anti–lamin A/C antibody from cells generated in (G). Quantitation of abnormal nuclear structures (**I**) or circularity (**J**) from cells in (H). Data represent average and SEM from three independent experiments. Scale bars, 10 μm. $^{**}P < 0.001$.

that UbcH7 may not directly connect to the nuclear envelope. Overexpressing Chk1 or 53BP1, two known UbcH7 substrates (*32*–*34*), did not cause the same nuclear structural abnormalities as shown in UbcH7-depleted cells (*32*, *33*), suggesting that these two substrates were not responsible for the nuclear structure regulation by UbcH7. Because UbcH7 is a cytoplasmic ubiquitin E2 enzyme that controls protein stability, we hypothesized that UbcH7 regulates the nuclear morphology through controlling the expression levels of protein(s) involved in the maintenance of the LINC–nuclear envelope structure. To this end, we performed both stable isotope labeling with amino acids (SILAC) and RNA sequencing to identify cytosol-nucleus structural genes whose protein, but not mRNA levels, was greatly increased by UbcH7 depletion (tables S1 and S2). These analyses revealed three cytoskeletal genes encoding tubulin 4A, MYO10, and synemin as strong candidates, because their protein, but not mRNA levels, was significantly increased in UbcH7-depleted cells (Fig. 2A).

To confirm these mass spectrometric results, we treated control or UbcH7-depleted A549 cells with cycloheximide (CHX) to block the de novo protein synthesis and measured protein degradation over time. As a positive control of UbcH7's substrate (*32*, *34*), Chk1 was stabilized when UbcH7 was depleted (Fig. 2B). We found that both the basal level and the protein stability of MYO10, but not those of tubulin 4A or synemin, were greatly increased in UbcH7-depleted A549 (Fig. 2B) and HeLa (fig. S3, A and B) cells compared to control cells. These data suggest MYO10 as a potential substrate for UbcH7. The increases in tubulin 4A and synemin in SILAC may be caused by nonspecific effects in that particular experiment.

Depletion of UbcH7 also increased the basal level of MYO10 in MCF7, U2OS, MEF, and WI38 cells (fig. S3C), suggesting the generality of the role of UbcH7 in regulating the MYO10 protein level. Then, to understand whether MYO10 degradation is proteasome dependent, we cotreated A549 control and UbcH7-depleted cells with CHX and the proteasome inhibitor MG132 (*N*-carbobenzyloxy-L-leucyl-L-leucyl-L-leucinal). We found that MG132 completely suppressed CHX-induced MYO10 degradation in control cells, whereas the effect of CHX and MG132 was weaker in UbcH7-depleted cells (Fig. 2C). These data confirm MYO10 as an unstable protein that undergoes proteasome-dependent degradation. Consistently, endogenous MYO10 interacted with endogenous UbcH7 in A549 parental cells, which was abolished by UbcH7 depletion (Fig. 2D). Similar coimmunoprecipitation (co-IP) was observed for exogenous proteins (Fig. 2E).

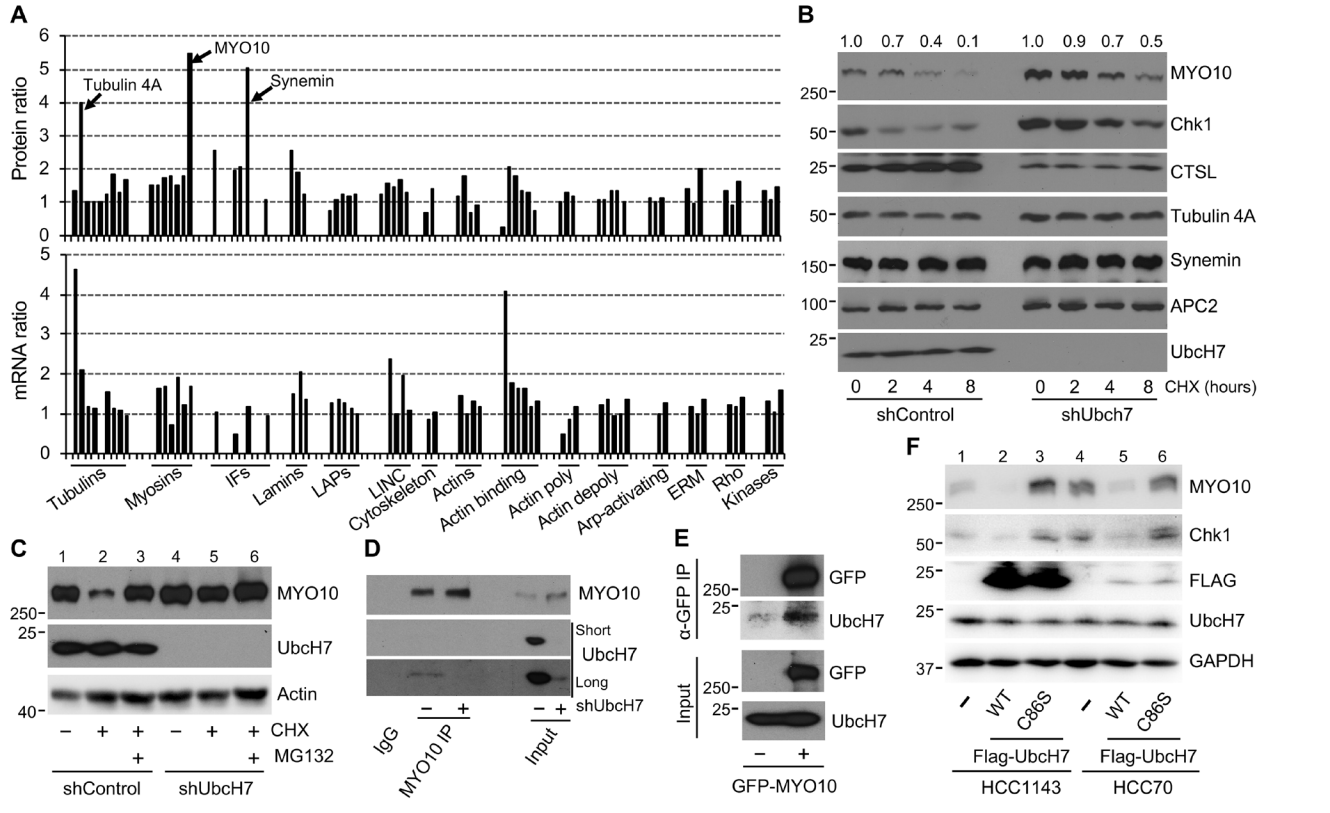

Fig. 2. Identification of MYO10 as an UbcH7 substrate. (**A**) Summary of SILAC (top) and RNA sequencing (bottom) data for cytosolic and nuclear structural genes in UbcH7-depleted cells relative to parental A549 cells. Gene families are indicated below. IFs, intermediate filaments; LAPs, lamin-associating proteins; ERM, actin-linkage to membrane. (**B**) A549 control or UbcH7-depleted cells were treated with 320 μM CHX for indicated times, and protein expression was examined by specific antibodies. The band intensity of MYO10 was quantitated and shown above. (**C**) A549 parental and UbcH7-depleted cells were treated with 320 μM CHX with or without 15 μM MG132 for 6 hours, and protein expression was examined. (**D**) Parental and UbcH7-depleted A549 cells were immunoprecipitated (IPed) with rabbit immunoglobulin G (IgG) or rabbit anti-MYO10 antibodies and blotted with indicated antibodies. Short and long exposures for the UbcH7 blot were shown. (**E**) Human embryonic kidney (HEK) 293T cells were transfected with GFP-MYO10 for 48 hours, IPed with the rabbit anti-GFP antibody, and blotted with indicated antibodies. Ten percent of input was also run (bottom). (**F**) Breast cancer HCC1143 and HCC70 cells were transfected with Flag-UbcH7 wild type (WT) or the C86S mutant for 48 hours, and protein expression was examined using specific antibodies.

If UbcH7 indeed regulates MYO10 degradation, then overexpression of which should reduce the protein level of MYO10. To this end, we overexpressed Flag-UbcH7 WT or the catalytically dead C86S mutant in two breast cancer cell lines, HCC1143 and HCC70, and examined the protein level of endogenous MYO10. The results show that while overexpression of Flag-UbcH7 WT reduced the level of MYO10, the C86S mutant actually increased it in HCC1143 cells (Fig. 2F). Such an increase is consistent with the idea that C86S is a dominant negative mutant of UbcH7 as we previously reported (*32*). The effect of the C86S mutant on HCC70 cells was weaker than on HCC1143 cells, likely because of less overexpression of the mutant protein. Together, these data confirm MYO10 as a substrate of UbcH7.

If MYO10 is indeed responsible for the nuclear structural abnormalities caused by UbcH7 depletion, then we would have the following predictions. First, overexpression of MYO10 alone should induce the same abnormal nuclear structures as caused by UbcH7 depletion; second, reducing the elevated level of MYO10 should rescue the abnormal nuclear morphology induced by UbcH7 depletion. To this end, we first overexpressed MYO10 in A549 cells, as this cell line has a relatively low basal level of abnormal nuclear structure (<10%). We found that overexpression of green fluorescent protein (GFP)–MYO10 indeed significantly increased the percentage of cells with abnormal nuclear structures (fig. S4, A and B, arrows). To better determine the impact of MYO10 expression levels on the nuclear morphology, we intended to overexpress different levels of GFP-MYO10 in U2OS cells with endogenous MYO10 deleted by CRISPR-Cas. Despite repeated attempts, we only obtained *MYO10*$^{+/-}$ clones, probably because *MYO10*$^{-/-}$ clones will not grow although *Myo10*$^{-/-}$ MEFs survived (*35*). However, the *MYO10*$^{+/-}$ clones expressed significantly reduced levels of MYO10 proteins compared with parental cells (Fig. 3A), allowing us to stably reexpress different levels of GFP-MYO10 in these clones (Fig. 3A). Genomic DNA sequencing revealed that U2OS cells likely contained multiple copies of *MYO10* genes, and CRISPR-Cas deleted most of them with only one allele

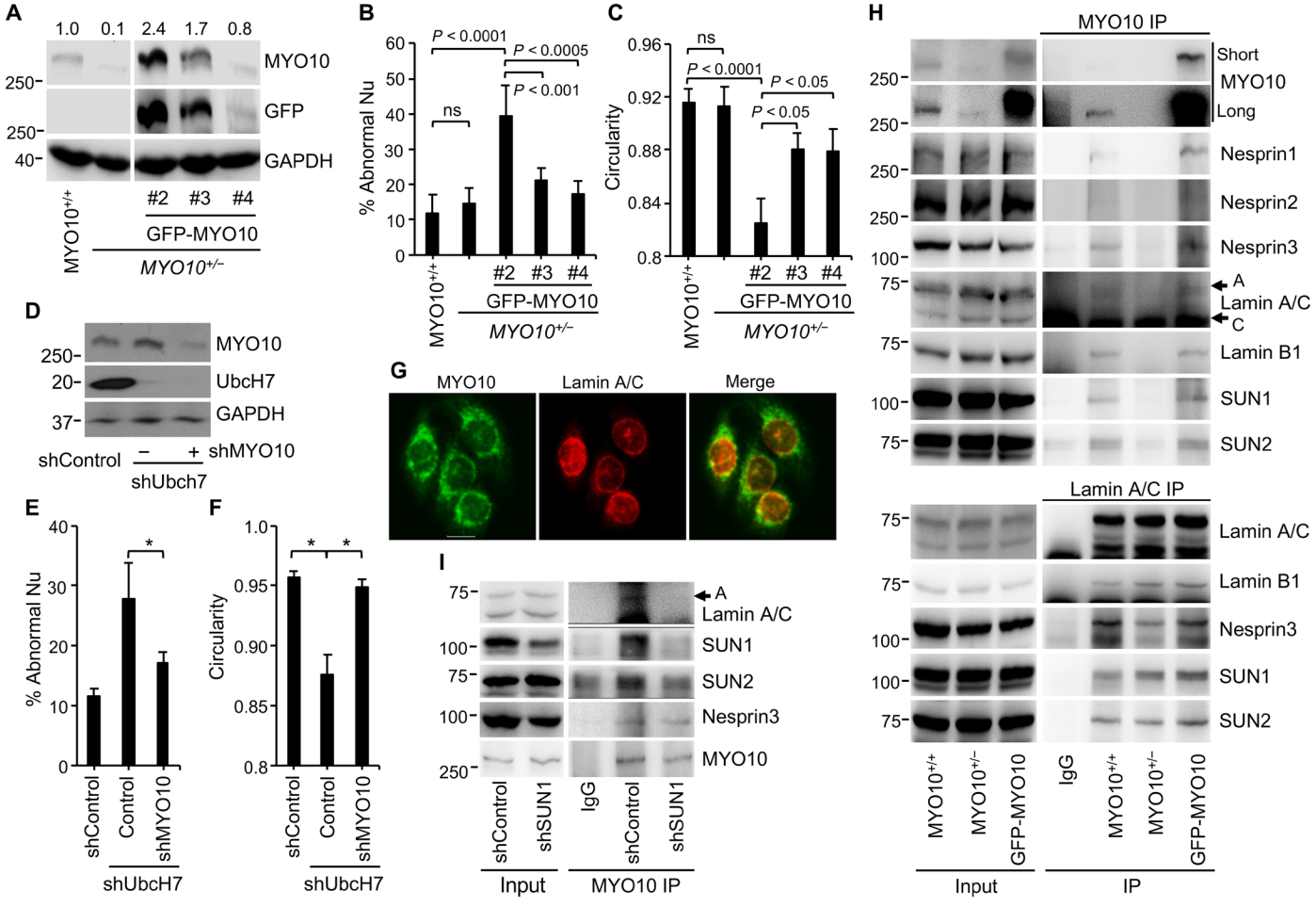

Fig. 3. MYO10 regulates the nuclear structural morphology. (**A**) U2OS parental, *MYO10*$^{+/-}$, and *MYO10*$^{+/-}$ cells stably expressing different levels of GFP-MYO10 (clones #2 to 4). Quantitation of MYO10 protein levels is shown above from three replicates. Quantitation of abnormal nuclear structures (**B**) or cellular circularity (**C**) from cells in (A). (**D**) UbcH7-depleted A549 cells were infected with lentivirus shRNA targeting *MYO10* for indicated times, and protein expression was examined. Quantitation of abnormal nuclear structures (**E**) or cellular circularity (**F**) from cells in (D). (**G**) Parental A549 cells were stained with antibodies against MYO10 and lamin A/C. Representative images are shown. Scale bar, 10 μm. (**H**) U2OS parental, *MYO10*$^{+/-}$, and *MYO10*$^{+/-}$ cells stably expressing GFP-MYO10 (clone #3) were IPed with MYO10 or lamin A/C and blotted with indicated antibodies. Inputs (5%) from parallel cell samples were run for protein expression. Short and long exposures for MYO10 are provided. (**I**) A549 control or SUN1-depleted cells were IPed with the anti-MYO10 antibody and blotted with indicated antibodies. Data represent average and SEM from three replicates. *$P < 0.05$. ns, not significant.

left (fig. S5), consistent with the greatly reduced protein level of the $MYO10^{+/-}$ clone. Because the basal level of abnormal nuclear structure in U2OS parental cells is also low (<10%), a reduction in MYO10 rarely altered the percentage of cells with abnormal nuclear morphology (Fig. 3B). However, introducing GFP-MYO10 into $MYO10^{+/-}$ U2OS cells dose-dependently increased the rate of abnormal nuclear structures (Fig. 3B) and reduced nuclear circularity (Fig. 3C). These results suggest that MYO10 causes abnormal nuclear structures in a protein expression level–dependent manner.

Second, when we transiently infected UbcH7-depleted A549 cells with short hairpin RNA (shRNA) targeting *MYO10* to reduce the elevated level of MYO10 in these cells (Fig. 3D), we observed a significant inhibition of the nuclear structural abnormality induced by UbcH7 depletion (Fig. 3, E and F). Further, depletion of UbcH7 resulted in increases in both MYO10 levels and abnormal nuclear structures in another nontransformed cell line, the human retinal pigment epithelial ARPE19 (fig. S6, A to D), further confirming the general role of UbcH7 in regulating the nuclear structure and MYO10 expression. Together, these lines of findings suggest that MYO10 is a major factor that contributed to the nuclear structural regulation of UbcH7 and that the protein level of MYO10 is critical for this function.

MYO10 regulates the nuclear structural integrity through the LINC complex

Then, we asked how MYO10 regulates the nuclear structure integrity. MYO10 proteins are mainly localized in the cytoplasm; however, unlike UbcH7, MYO10 also accumulated at the perinuclear region that wraps around the nuclear envelope (Fig. 3G), indicating that MYO10 may directly interact with the LINC–nuclear envelope complex. To test this idea, we used the $MYO10^{+/-}$ U2OS cells and the derivative clone expressing approximately twofold GFP-MYO10 to perform co-IP. We observed complex formation between endogenous MYO10 and LINC proteins including Nesprin1/3 and SUN1/2, as well as lamin A and B, in parental cells (Fig. 3H, IP, top), suggesting that MYO10 indeed associated with the LINC–nuclear envelope network. We did not detect lamin C in the anti-MYO10 IP (Fig. 3H, IP, top) with unknown reasons at this moment. The association of MYO10 with all these proteins was not detected in $MYO10^{+/-}$ cells, whereas reconstitution with GFP-MYO10 restored the interaction (Fig. 3H, IP, top), suggesting that the interaction is specific to MYO10.

Depletion of MYO10 did not affect the interaction between lamin A/C and SUN1/2 (Fig. 3H, IP, bottom), the nuclear portion of the LINC complex (*8*); however, it reduced the association between lamin A/C and Nesprin3 (Fig. 3H, IP, bottom), the outer nuclear membrane portion of the LINC complex that extends to the cytoplasm (*8*), which was restored in MYO10-reconstituted cells (Fig. 3H, IP, bottom). Similarly, depletion of SUN1 (Fig. 3I, input) markedly reduced the association between MYO10 and lamin A or SUN1/2 but not with Nesprin3 (Fig. 3I, IP). These results suggest a model in which MYO10 associates with the nuclear envelope through Nesprins and then the SUN component of the LINC complex. An extension of this hypothesis is that alterations in MYO10 disrupt/reduce the proper cellular localization of Nesprins to the outer nuclear membrane, leading to impaired LINC complex assembly and, consequently, reduced association of MYO10 or Nesprins with SUNs or lamins.

To test this hypothesis, we first examined cellular localization of MYO10 and Nesprin3. In parental A549 and MDA-MB-231 cells, MYO10 and Nesprin3 nearly completely colocalized at the perinuclear region (figs. S7B and S8A). Depletion of Nesprin3 (fig. S7A) disrupted the regular perinuclear localization pattern of MYO10 (fig. S7B). The other way around was also true, meaning that deletion of MYO10 in MDA-MB-231 cells (also created by CRISPR-Cas) resulted in disoriented cellular localization of Nesprin3, which showed much less regular perinuclear staining (fig. S8A). These results suggest that the expression levels of MYO10 and Nesprin3 are important for each other's proper perinuclear localization; hence, when MYO10 was depleted, the fraction of Nesprin3 that is correctly inserted into the outer nuclear envelope region was reduced, leading to a reduction/disruption in its association with SUN proteins and then lamin A/C without affecting the interaction between lamin A/C and SUN1. In agreement with this idea, we found that, in Nesprin3-depleted cells, MYO10 also interacted less with SUN1 or lamin A/C (fig. S8B), similar to the observations seen in MYO10-depleted cells (Fig. 3, H and I). These data support a model in which MYO10 localizes to the perinuclear region and associates with the nucleus through the Nesprin component of the LINC complex.

β-TrCP1 is the E3 ligase controlling MYO10 protein stability

Given the importance of MYO10 protein level in the regulation of nuclear morphology, we then decided to determine the E3 ligase for MYO10 degradation. MYO10 was previously identified as an interacting protein for human β-TrCP1 by mass spectrometry (*36*–*38*); however, no biochemical study has been reported to confirm this interaction and to demonstrate its biological implications. β-TrCP1 is one of the 69 human F-box proteins that act as the substrate recognition component of the SCF (Skp1–Cullin–F-box) type E3 ligase (*39*). The $SCF^{\beta\text{-}TrCP}$ complex regulates a wide variety of biological functions including cancer in vertebrates through mediating the stability of a long list of protein substrates including β-catenin, inhibitor of nuclear factor κB (NF-κB), Cdc25A, Emi1, and Deptor [reviews in (*39*, *40*)]. To determine whether β-TrCP1 is an E3 ligase for MYO10 degradation, we first asked whether they interact. For this purpose, we used the human embryonic kidney (HEK) 293T cell line to perform co-IP, as this cell line allows high level of expression of exogenous proteins. We found that GFP-MYO10 indeed associated with Flag–β-TrCP1 or Flag-Cul1 (Fig. 4A). The F-box–deleted β-TrCP1 (Flag-TrCP1-ΔF) also co–immunoprecipitated (IPed) with GFP-MYO10 (Fig. 4B), consistent with the idea that the F-box does not affect the binding between β-TrCP1 and its substrate (*41*). Endogenous MYO10 also formed a complex with endogenous Cul1 or β-TrCP1 in A549 cells (Fig. 4C), and depletion of UbcH7 slightly reduced the interaction between MYO10 and Cul1 or β-TrCP1 (Fig. 4C).

We then overexpressed Flag-TrCP1 or Flag-TrCP1-ΔF in HEK293T cells, treated the cells with CHX for 0, 3, and 6 hours, and examined the protein level of endogenous MYO10. The results show that overexpression of Flag-TrCP1 greatly accelerated MYO10 degradation, whereas Flag-TrCP1-ΔF partially reduced it (Fig. 4, D and E), as β-TrCP1–ΔF is a dominant negative mutant for endogenous β-TrCP1. To confirm the role of β-TrCP1 in MYO10 degradation, we depleted β-TrCP1 by a small interfering RNA (siRNA) SMARTpool in A549 cells and examined MYO10 protein stability. Depletion of β-TrCP1 not only greatly increased the basal level but also significantly enhanced MYO10 protein stability (Fig. 4, F and G). Co-depletion of UbcH7 and β-TrCP1 showed an additive effect in increasing the protein level of MYO10 (fig. S3D). Further, we found that, while β-TrCP1 increased MYO10 ubiquitination, the

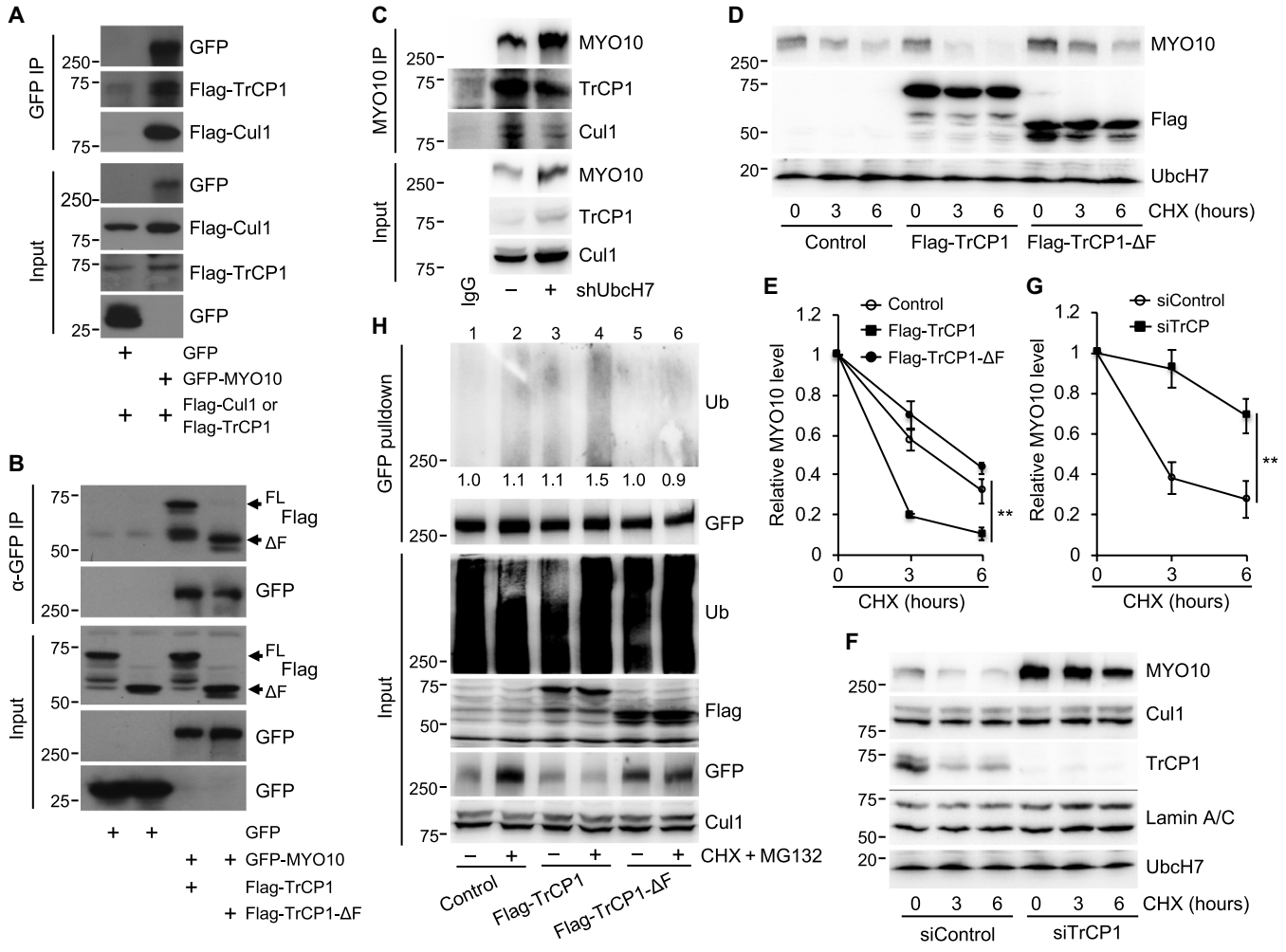

Fig. 4. β-TrCP1 regulates MYO10 ubiquitination and degradation. (**A**) HEK293T cells were transfected with GFP, GFP-MYO10, and FLAG–β-TrCP1 or FLAG-Cul1 for 48 hours, IPed with the anti-GFP antibody, and blotted with indicated antibodies. Ten percent of input was run to show protein expression. (**B**) HEK293T cells were transfected with GFP, GFP-MYO10, and FLAG-β-TrCP1–FL (full-length) or FLAG-β-TrCP1–ΔF (F-box deleted) for 48 hours; IPed with the anti-GFP antibody; and blotted with indicated antibodies. Five percent of input was run to show protein expression. (**C**) A549 control or UbcH7-depleted cells were IPed with anti-MYO10 and blotted with antibodies for endogenous proteins. Input (5%) was also run for loading control. (**D**) HEK293T cells were transfected with FLAG–β-TrCP1 or FLAG-β–TrCP1–ΔF for 48 hours and treated with 320 μM CHX for indicated times, and protein expression was examined by specific antibodies. (**E**) The band intensity of MYO10 in (D) was quantitated using the ImageJ software and normalized to that of the 0-hours group. (**F**) A549 cells were transfected with siRNA control or targeting β-TrCP1 for 48 hours and treated with 320 μM CHX for indicated times, and protein expression was examined by specific antibodies. (**G**) Quantitation of MYO10 band intensity in (F) from three replicates. (**H**) HEK293T cells were transfected with FLAG–β-TrCP1 or FLAG-β–TrCP1–ΔF with His-Ub for 48 hours, treated with 320 μM CHX and 15 μM MG132 for 6 hours, lysed cells under denaturing conditions, and proceeded to detect MYO10 ubiquitination as described previously (*75*). Ten percent of input was run for loading control. The band intensity of ubiquitinated MYO10 in the IP was quantitated by ImageJ from three blots and presented as average relative intensity (numbers below), which showed a statistical significance ($P = 0.0042$) between lanes 2 and 4. Quantitation data are presented as average and SD from at least three experiments. $^{**}P < 0.0001$.

β-TrCP1–ΔF mutant reduced it (Fig. 4H, compare lanes 2, 4, and 6). Human β-TrCP2 shares similarities with β-TrCP1 in regulating protein stability (*39*, *40*); hence, β-TrCP2 might also play a redundant role in MYO10 degradation. Nonetheless, these studies identify β-TrCP1 as a major E3 ligase for MYO10 protein ubiquitination and degradation.

Because β-TrCP1 is the E3 ligase that controls MYO10 protein levels, we asked whether depletion of β-TrCP1 could also induce abnormal nuclear structures as seen in UbcH7-depleted or MYO10-overexpressing cells, although it was not mentioned in β-*Trcp1*–null mouse cells (*42*). To this end, we depleted β-TrCP1 by siRNA in A549 cells and found that β-TrCP1–depleted cells showed significantly increased nuclear structural abnormalities (fig. S9, A and B). These data support the role of MYO10 in regulating the nuclear morphology.

MYO10 regulates genome stability and cancer progression

Because intact nuclear structure plays a critical role in the maintenance of genome stability and therefore the prevention of cancer (*43*–*46*), our results suggest that MYO10 may regulate genome stability and cancer progression. Consistently, MYO10 was found to be amplified in a wide range of human cancers (fig. S10). Similarly,

we found a positive correlation between MYO10 protein levels and the aggressiveness of breast cell lines with highly malignant triple-negative breast cancer cell lines (e.g., MDA-MB-231, HCC1143, and HCC70) expressing the highest level of MYO10 (fig. S11A). MYO10 protein levels positively correlated with the extent of abnormal nuclear structures in these cell lines (fig. S11, B to D). To further corroborate this idea, we surveyed the mRNA levels of *Myo10* in paired control and mouse mammary tumor tissues driven by a known transgene, polyomavirus middle T antigen (PyMT) (*47*), and found that *Myo10* was significantly increased in all four stages of PyMT-induced hyperplasia and tumors compared with control mice (fig. S12A). We also examined the expression of *Btrc* and *Ubcm4*, the mouse genes for human *BTRC* (encoding β-TrCP1) and *UBE2L3* (encoding UbcH7), respectively, and found an overall inverse correlation between *Myo10* and *Btrc* in these tissues except at week 12; however, while the increases in *Myo10* were significant, the reduction in *Btrc* was not (fig. S12A). On the other hand, the level of *Ubcm4* barely changed (except a small increase at week 8) (fig. S12A), suggesting an important role of β-TrCP1 in MYO10 regulation.

To understand how MYO10 regulates cancer progression, we decided to determine the role of MYO10 in inducing genomic instability. We first asked whether MYO10 is responsible for causing the abnormal nuclear structures in aggressive breast cancer cells. To this end, we transiently depleted *MYO10* in highly metastatic HCC70 and HCC1143 cancer cell lines (Fig. 5A and fig. S11E) and found that these cells now had significantly reduced abnormal nuclear structures and improved nuclear morphology (Fig. 5, B and C), supporting the role of MYO10 in mediating the nuclear structure integrity. Deletion of MYO10 did not affect the localization of SUN1 in the nuclear envelope region (Fig. 5B). This is different from that of Nesprin3 (fig. S8A), further supporting the idea that MYO10 regulates the Nesprin portion of the LINC complex.

Subsequently, we found that *MYO10* depletion significantly reduced the percentage of HCC1143 cells with micronuclei (fig. S13, A and B), a common nuclear aberration that is also related to nuclear envelope defects and indicates genomic instability (*48*). The same is true for MDA-MD-231 cells (fig. S13, C and D). We observed a positive correlation between GFP-MYO10 expression levels and the

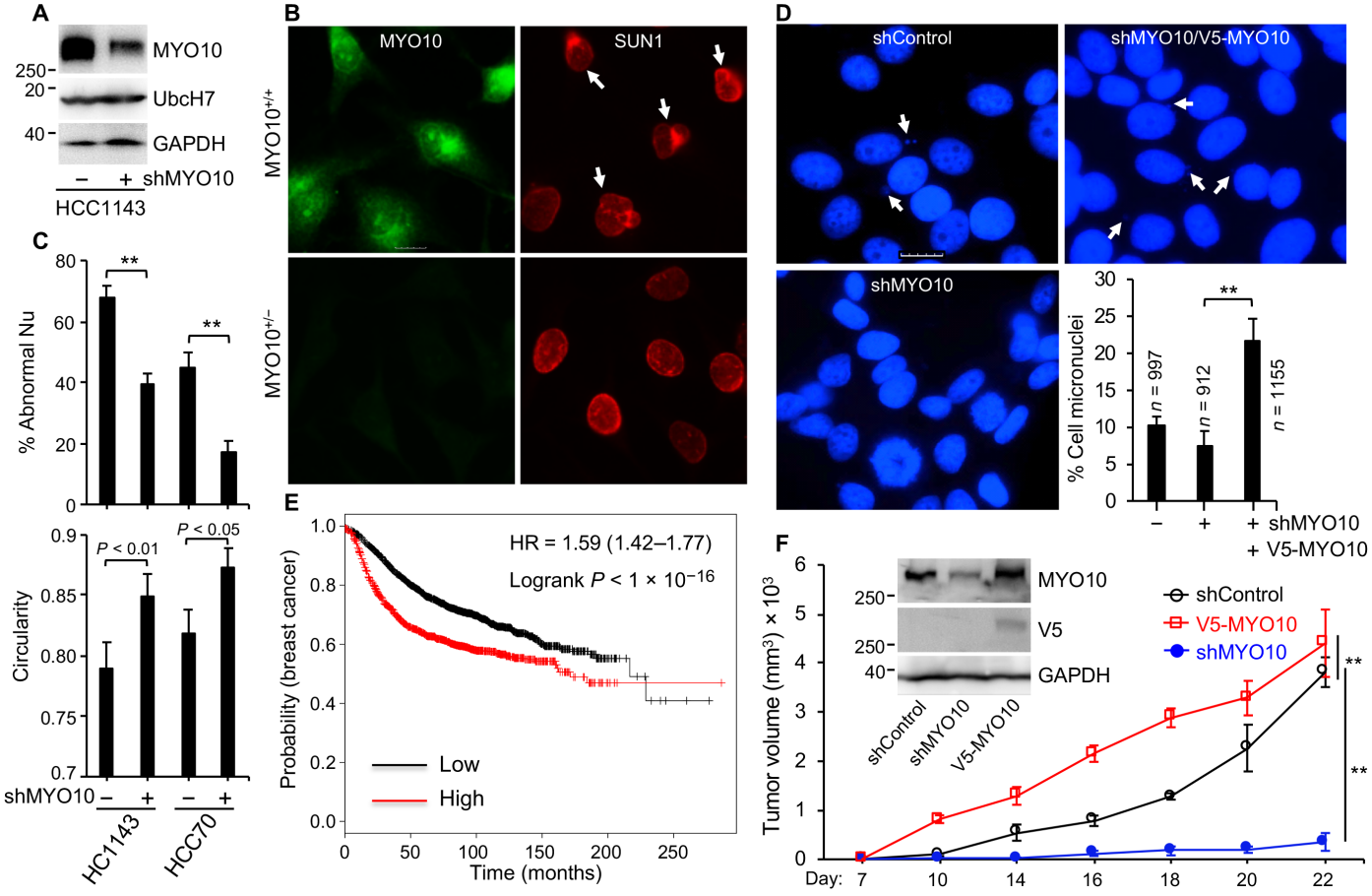

Fig. 5. Association of MYO10 with nuclear morphology in cancer cells. (**A**) HCC1143 cells were infected with shRNA lentivirus targeting MYO10, and stable clones were selected for protein expression. GAPDH, glyceraldehyde phosphate dehydrogenase. (**B**) MDA-MB-231 parental or MYO10$^{+/-}$ cells were stained for MYO10 and SUN1 antibodies. Arrows indicate abnormal nuclei. Scale bar, 10 μm. (**C**) Quantitation of cells with abnormal nuclear morphology (top) and cellular circularity (bottom) in (B). Data represent average and SEM from three independent experiments. (**D**) MCF7 parental, MYO10-depleted, or MYO10-depleted but reconstituted with V5-MYO10 cells were stained with 4′,6-diamidino-2-phenylindole (DAPI) for micronuclei. Representative images are shown. Arrows indicate micronuclei, and the quantitation is shown. Cell numbers counted are shown. (**E**) Kaplan-Meier survival of patients with breast cancer (pooled without subgrouping) expressing low or high *MYO10*. HR, hazard ratio. (**F**) HCC1143 parental, *MYO10*-depleted or V5-MYO10–overexpressing cells were inoculated into nude mice ($n = 5$), and tumor growth was monitored. MYO10 protein expression in tested cell lines was shown in the inset. Data represent average and SEM from three independent experiments unless otherwise indicated. **$P < 0.001$.

rate of micronuclei in U2OS *MYO10*$^{+/-}$ derivative cells (fig. S13E). For the less malignant MCF7 breast cancer cells, while depletion of MYO10 reduced the incidence of micronuclei, overexpressing V5-MYO10 to MYO10-depleted cells not only restored but also actually significantly increased the rate of micronuclei (Fig. 5D). These results suggest that MYO10 overexpression causatively increased the incidence of micronuclei. Consistently, MYO10 overexpression increased the percentage of abnormal mitosis in synchronized (fig. S13, F and G, isolated chromosomes) and asynchronized (fig. S14, A and B) cells. Metaphase spreading revealed a significant increase in a particular type of chromosomal abnormality (i.e., chromosome deletion) in cells overexpressing MYO10 (fig. S13, H and I). In line with increases in micronuclei and chromosomal alterations, MYO10-overexpressing cells had significantly elevated basal levels of phosphorylated histone H2A X variant (γH2AX) foci (fig. S13J), a marker indicating DNA damage, supporting elevated levels of genomic instability in MYO10^{high} or overexpressing cells.

Then, we asked how MYO10 regulates genomic instability. Given the data presented above, we hypothesize that MYO10 regulates genome stability through mediating mitosis progression via its physical association with the LINC complex. To test this idea, we first asked whether manipulating the LINC complex could ameliorate genomic instability caused by MYO10 overexpression. To this end, we first treated MYO10-overexpressing HCC1143 cells with four chemicals that can ameliorate nuclear structural abnormalities including lonafarnib, a farnesyltransferase inhibitor that has been approved by the U.S. Food and Drug Administration to treat patients with progeria characterized with abnormal nuclear structures. We observed a significant rescue of the abnormal nuclear structure in HCC1143 cells by three of the four compounds with lonafarnib showing the strongest effect (fig. S15, A and B). Second, we partially depleted SUN1 in HCC1143 parental or V5-MYO10–overexpressing cells (fig. S16A) and found significant improvement in nuclear structure abnormalities and micronuclei (fig. S16B). These results support the idea that MYO10^{high} or overexpression induces genomic instability through the LINC–nuclear envelope network. Subsequently, we determined the impact of MYO10 on mitosis progression using the engineered MYO10$^{+/-}$ U2OS cells. First, we synchronized parental and MYO10$^{+/-}$ cells at the G_1-S boundary, released them into the cell cycle, and monitored the mitosis progression. We observed a significant delay in mitosis progression in MYO10$^{+/-}$ cells (fig. S17, A and B). Second, we conducted live cell imaging and found that, again, MYO10$^{+/-}$ cells spent significantly longer time in mitosis than parental cells, which was completely rescued by reconstitution with GFP-MYO10 that was expressed at similar levels to endogenous proteins (Fig. 3A and fig. S17, C and D). Combined, these data suggest that MYO10^{high} or overexpression increases genomic instability through its role in mitotic regulation, and this requires its association with the LINC complex, but independent of the lamin proteins, the latter is consistent with previous studies (*49*).

Consistent with the role of MYO10 in inducing genomic instability, Kaplan-Meier analysis revealed that *MYO10* expression levels predisposed the overall survival of patients with breast cancer (Fig. 5E). These data are consistent with previous reports in breast (*26*, *30*) and skin (*29*) cancers. To further probe the role of *MYO10* in cancer progression, we generated HCC1143 breast cancer cell lines depleted of *MYO10* or overexpressing V5-MYO10 (Fig. 5F) and examined tumor growth in nude mice. The results show that overexpression of MYO10 significantly accelerated tumor growth in mice compared with parental cells (Fig. 5F). In contrast, depletion of *MYO10* significantly suppressed the tumor growth (Fig. 5F), similar to previously reported results (*26*, *30*) but with much stronger effect.

MYO10 regulates the tumor-promoting inflammatory response in cancer

While MYO10 depletion significantly blocked tumor growth in mice (Fig. 5F), it only slightly reduced HCC1143 cell proliferation in vitro (fig. S18). These results indicate that MYO10 is not essential for cell proliferation but instead may provide a tumor-promoting environment in vivo. Given that MYO10 overexpression led to a significantly elevated level of genomic instability (e.g., fragile nuclear structures, micronuclei, chromosome segregation defects, and chromosome deletions) and genomic instability can activate the cGAS/STING pathway (*12*), we asked whether MYO10 regulates the cGAS/STING-dependent inflammation in cancer.

By examining protein expression levels, we found a positive correlation between MYO10 and STING, pTBK1 (TANK binding kinase 1), or pSTAT1/3 (signal transducer and activator of transcription 1/3) in various breast cancer cell lines (Fig. 6A). Depleting *MYO10* greatly reduced the levels of STING, pTBK1, pSTAT1/3, and interleukin-1β (IL-1β) in the malignant HCC70 breast cancer cells (Fig. 6B). Consistently, MYO10 depletion significantly reduced the level of cyclic guanosine monophosphate–adenosine monophosphate (cGAMP) (Fig. 6C), the messenger that activates STING, in these cancer cells. Similarly, the levels of interferon (IFN)–stimulated genes and NF-κB target genes (such as *IFNB1* and *IL-1*β), but not the DNA damage response gene *CDKN1A*, were significantly reduced in MYO10-depleted HCC70 cells (fig. S19, A to C). Further, we monitored nuclear localization of IFN regulatory factor 3 (IRF3) phosphorylated at Ser^{386}, which is carried out by TBK1 during the activation of the cGAS/STING pathway (*50*). Nuclear localization of pIRF3 was readily detected in MYO10^{high} HCC1143 parental cells (fig. S19D), consistent with the relatively high basal level of inflammation in this cell line (Fig. 6A). While depletion of MYO10 reduced the nuclear signal of pIRF3, overexpression of MYO10 greatly enhanced it (fig. S19D). These results support the idea that MYO10 regulates the inflammatory response.

As *MYO10* is overexpressed in human cancers (fig. S10), we asked whether overexpressing MYO10 would then enhance the inflammatory response. To this end, we collected cytosolic and nuclear extracts from V5-MYO10 stably expressing MDA-MB-231 breast cancer cells and examined expression of proteins involved in the cGAS/STING pathway. The results show that MYO10 overexpression increased the protein levels of STING, IL-1β, IL-8, and pSTAT3, especially in the nuclear fraction (Fig. 6D). No changes in the total level of P65 were observed; however, there was a clear increase and decrease in the nuclear and cytoplasmic pools of P65, respectively (Fig. 6D), indicating translocation of P65 into the nucleus by MYO10 overexpression. Nuclear translocation of P65 is widely accepted as a marker for activation of the NF-κB signaling and inflammation (*51*). Hence, these data suggest that MYO10 overexpression increases the cGAS/STING-mediated inflammatory response at least partially through the NF-κB signaling.

Aspirin is a nonsteroid anti-inflammation drug that has been used to treat inflammation through inhibiting the cyclooxygenase (*52*). A recent study suggested that aspirin could inhibit the cGAS/STING pathway through acetylating cGAS to prevent its DNA binding (*53*).

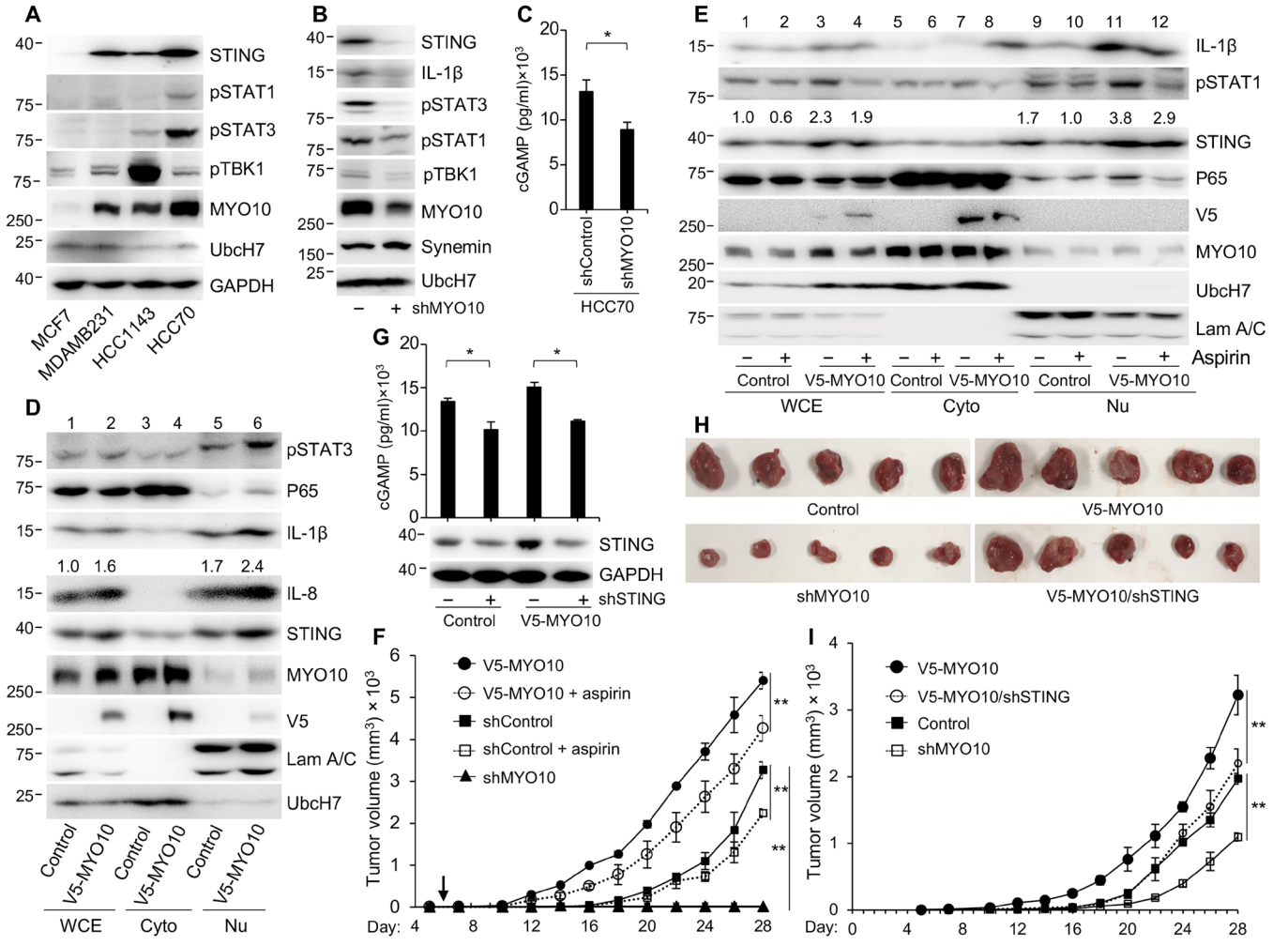

Fig. 6. MYO10 regulates inflammatory response and cancer progression. (**A**) Equal amounts of total proteins from different breast cancer cell lines were run on SDS–polyacrylamide gel electrophoresis (SDS-PAGE) and blotted with indicated antibodies. (**B**) HCC70 parental or MYO10-depleted cells were collected and blotted with indicated antibodies. (**C**) The level of cGAMP in HCC70 parental and MYO10-depleted cells were measured by enzyme-linked immunosorbent assay (ELISA). (**D**) MDA-MB-231 parental or V5-MYO10–overexpressing cells were fractionated into cytosolic (cyto) and nuclear (Nu) extracts and blotted with indicated antibodies. Whole-cell extracts (WCE) were also examined for protein expression. (**E**) MDA-MB-231 parental or V5-MYO10–overexpressing cells were treated or not with 3 μM aspirin for 24 hours, fractionated into cytosolic and nuclear extracts, and blotted with indicated antibodies. Protein expression in WCE was also monitored. (**F**) HCC1143 parental, *MYO10* stably depleted, or V5-MYO10–overexpressing cells were inoculated into NOD-SCID mice. At day 5, parental or V5-MYO10 mice were randomly separated into two groups ($n = 5$), and one group received daily aspirin (30 mg/kg) by oral gavage. (**G**) The level of cGAMP in HCC1143 parental, *MYO10*-depleted, V5-MYO10–overexpressing, or V5-MYO10–overexpressing but stably depleted of STING cells. The bottom panel shows the expression level of STING. These HCC1143 cells in (G) were inoculated into the mammary fat pad of nude mice and observed for tumor growth for 3 weeks. Tumors at the end of the experiment (**H**) and the growth curve (**I**) are shown. Data represent averages and SEM from at least three replicates except tumor studies. $^{**}P < 0.0001$ and $^{*}P < 0.05$.

We then asked whether aspirin could reduce inflammation caused by MYO10 overexpression. The results show that aspirin reduced the increases in the levels of STING, IL-1β, and pSTAT3 induced by MYO10 overexpression (Fig. 6E). Aspirin also inhibited the increase in the level of nuclear P65 in MYO10-overexpressing cells (Fig. 6E). These data confirm that aspirin inhibited the elevated inflammatory response caused by MYO10 overexpression. To further probe the significance of MYO10 overexpression–induced inflammation in cancer, we inoculated parental, MYO10 knockdown, or V5-MYO10–overexpressing HCC1143 breast cancer cells into non-obese diabetic–severe combined immunodeficient (NOD-SCID) mice and orally administered aspirin (30 mg/kg) daily to mice starting from day 5. Again, MYO10 depletion significantly blocked tumor growth, whereas its overexpression significantly accelerated the growth of this triple-negative breast cancer (Fig. 6F). Aspirin treatment significantly reduced the growth of both parental and MYO10-overexpressing tumors (Fig. 6F). Further, to confirm the importance of the cGAS/STING-dependent inflammation in MYO10-promoted tumor growth, we stably depleted STING in V5-MYO10–overexpressing HCC1143 breast cancer cells. We found that even a partial reduction in STING significantly reduced the level of cGAMP in cultured cancer cells (Fig. 6G) and inhibited tumor growth in mice compared with V5-MYO10–overexpressing cancer cells (Fig. 6, H and I). Together, these results confirm the importance of the cGAS/STING-mediated inflammatory pathway in $MYO10^{high}$- or overexpression-promoted tumor growth.

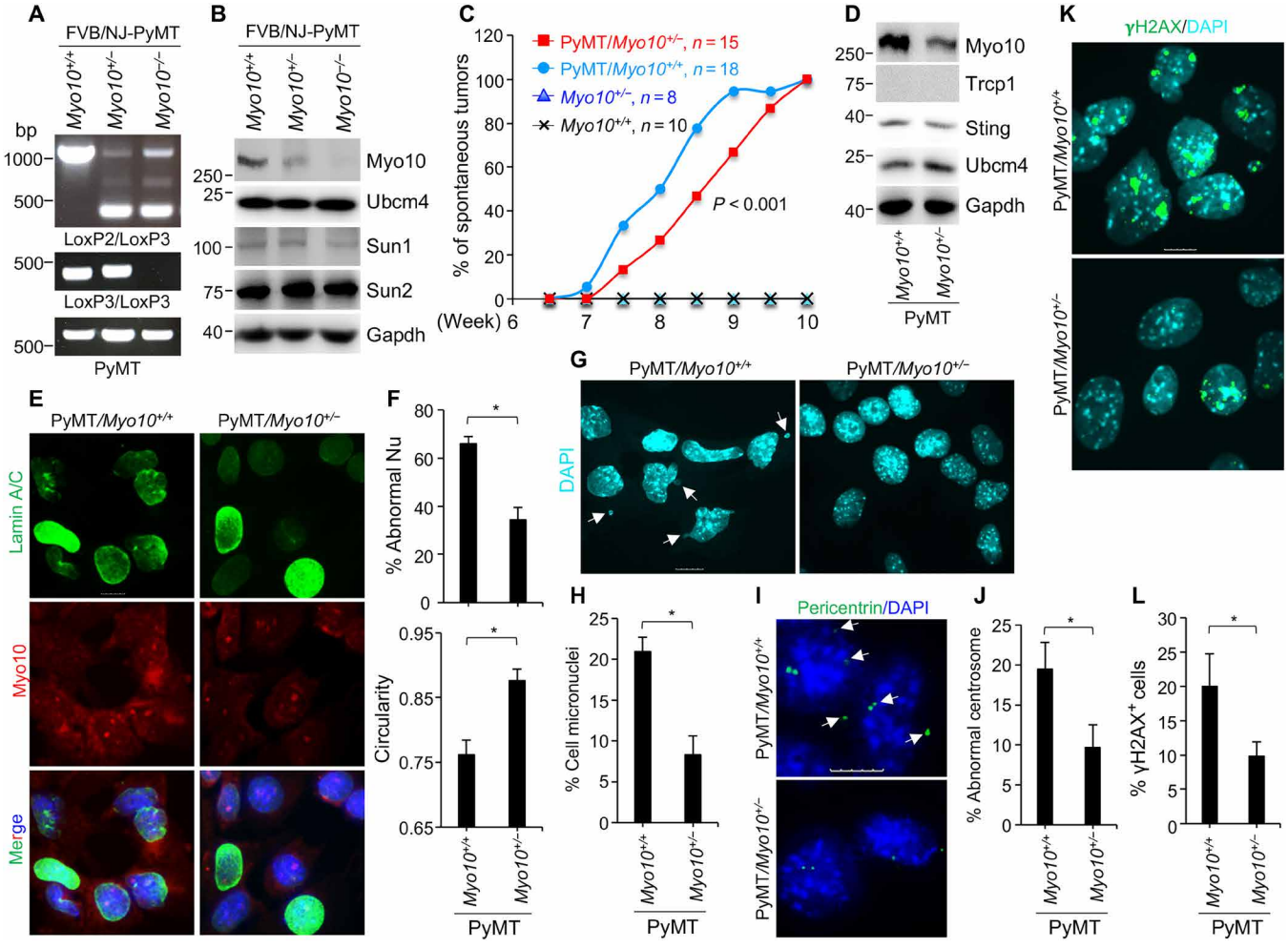

Fig. 7. MYO10 regulates tumor growth in immune-competent mice. (**A**) Genotyping of PyMT/*Myo10* mice. bp, base pair. (**B**) Protein expression from muscles obtained from PyMT/*Myo10*$^{+/+}$, PyMT/*Myo10*$^{+/-}$, and PyMT/*Myo10*$^{-/-}$ mice. (**C**) Percentage of spontaneous tumor occurrence from indicated female mice. (**D**) Freshly isolated tumor cells from the PyMT/*Myo10*$^{+/+}$ and PyMT/*Myo10*$^{+/-}$ female mice were analyzed for protein expression, as well as the following analyses. (**E**) Isolated tumor cells were stained for lamin A/C and Myo10. Representative images are shown. Scale bar, 100 μm. (**F**) Quantitation of tumor cells with abnormal nuclear morphology (top) and cellular circularity (bottom) from at least 50 cells in (E). (**G**) Freshly isolated tumor cells were stained with DAPI, and representative images are shown. Arrows indicate micronuclei. Scale bar, 10 μm. (**H**) Quantitation of tumor cells with micronuclei from at least 50 cells in (G). (**I**) Freshly isolated tumor cells were stained for pericentrin and DNA. Representative images are shown. Arrows indicate cells with abnormal number of centrosomes. Scale bar, 10 μm. (**J**) Quantitation of tumor cells with abnormal centrosomes in (I). (**K**) Freshly isolated tumor cells were stained with γH2AX and DAPI. Representative images are shown. Scale bar, 10 μm. (**L**) Percentage of tumor cells with ≥5 γH2AX foci in (I). Except (C), data represent average and SEM from at least three replicates.

To further determine the effect of MYO10 on tumor progression in an immune-competent background, we rederived *Myo10*$^{-/-}$ mice from the C57BL/6 strain (*35*) to the FVB/N background (Fig. 7A) and crossed it with transgenic mice that express the oncogene PyMT. PyMT female mice developed palpable mammary tumors with a mean latency of 53 days (*54*), allowing for rapid analysis of the impact of MYO10 on breast tumorigenesis, development, and therapy. We confirmed the depletion of Myo10 proteins in the knockout mice (Fig. 7, A and B). We figured that these mouse models could serve as useful tools to further test the relationship among β-TrCP1, MYO10, and UbcH7 in vivo. To this end, we examined protein levels of *Myo10*, β-*Trcp1*, and *Ubcm4* in the mammary gland from normal FVB/NJ, FVB/NJ-PyMT/Myo10$^{+/+}$, and FVB/NJ-PyMT/Myo10$^{+/-}$ mice. Intriguingly, we found that the protein level of β-Trcp1 was almost completely gone in PyMT mice, which correlated inversely with significantly elevated levels of Myo10; in contrast, the level of Ubcm4 barely changed (fig. S12B). Mouse mammary tumor virus (MMTV)–PyMT mice express reduced mRNA level of *Btrc* (fig. S12A); however, it is unclear whether such a relatively minor reduction in the mRNA level could contribute to an almost complete loss of the protein in these mice, which will be further investigated in future studies. Nonetheless, these results confirm the inverse correlation between MYO10 and β-TrCP1 in animals.

Subsequently, we analyzed tumor development in these mice. While deletion of one allele of *Myo10* did not induce spontaneous tumor in mice, it significantly delayed the onset of PyMT-induced breast tumor (Fig. 7C). The inhibitory effect of *Myo10*$^{+/-}$ was stronger than several factors that are known to be involved in PyMT-induced tumorigenesis including c-Src, Fak, and ErbB3, depletion of one allele of which failed to suppress PyMT-induced breast tumorigenesis

(*55*–*57*). Complete loss of *Myo10* led to about 50% embryonic lethality (*29*, *35*), which limited us to obtain enough number of PyMT/*Myo10*$^{-/-}$ female mice. Given that MYO10 depletion slowed glioma proliferation and prolonged mice survival (*58*), we would predict that *Myo10*$^{-/-}$ might further delay tumor development driven by PyMT, which will be examined when enough PyMT/*Myo10*$^{-/-}$ female mice could be obtained. Nonetheless, the significant inhibition of PyMT tumor in heterozygous *Myo10*$^{+/-}$ mice strongly supports the role of MYO10 in promoting breast tumorigenesis.

These engineered mouse models provide us great tools to assess the impact of MYO10 on genome stability regulation in vivo. To this end, we freshly isolated tumor cells from PyMT/*Myo10*$^{+/+}$ and PyMT/*Myo10*$^{+/-}$ mice (Fig. 7D) and evaluated genomic instability in the primary passage of these mouse tumor cells. First, there was a significant improvement in the nuclear morphology of tumor cells from the PyMT/*Myo10*$^{+/-}$ mice compared with PyMT/*Myo10*$^{+/+}$ mice (Fig. 7, E and F). Second, we observed a significant reduction in the percentage of cells with micronuclei in tumor cells from the PyMT/*Myo10*$^{+/-}$ mice (Fig. 7, G and H). Third, there was a significant improvement in centrosome number abnormalities in PyMT/*Myo10*$^{+/-}$ mice (Fig. 7, I and J). Last, tumor cells from the PyMT/*Myo10*$^{+/-}$ mice had significantly reduced levels of γH2AX foci (Fig. 7, J to L). Together, these data indicate that reducing the expression level of *Myo10* significantly ameliorated genomic instability in mouse tumors driven by the PyMT oncogene, supporting our observations seen in cultured human cancer cells.

MYO10 regulates cancer ICB therapy

Recent studies suggest that genomic instability could enhance the effect of tumor immune therapy (*14*, *59*) and predisposes patients with cancer to immunotherapy, including anti–programmed cell death 1 (PD-1) monotherapy in breast cancer (*60*, *61*). We showed that MYO10^{high} or overexpression greatly elevated the level of genomic instability in both human and mouse breast tumors. Hence, we asked whether MYO10^{high} or overexpression creates an immunogenic environment that responds to ICBs. To this end, we initiated the treatment of PyMT/*Myo10*$^{+/+}$ and PyMT/*Myo10*$^{+/-}$ mice with anti–PD-1 antibodies at around week 5.5 of age before the appearance of the first tumor and continued the injection until the age of week 13. First, for treatment-naïve mice, the tumor size of the first appearing tumor in PyMT/*Myo10*$^{+/-}$ mice was much smaller than that in PyMT/*Myo10*$^{+/+}$ mice (Fig. 8A), consistent with the idea that MYO10^{high} promotes tumor growth. However, while the anti–PD-1 antibody significantly inhibited tumor growth in PyMT/*Myo10*$^{+/+}$ mice, it failed to do so in PyMT/*Myo10*$^{+/-}$ mice (Fig. 8A). Rather, tumors in PyMT/*Myo10*$^{+/-}$ mice grew even larger in the presence of ICBs (Fig. 8A), suggesting that reducing MYO10 level induced resistance to ICBs.

To understand how these tumors responded differently to ICBs, we first measured type I IFNα (Ifnα) in tumors from these mice because, unlike type II IFNγ that can only be secreted by T and natural killer cells, type I IFNα can be secreted by all types of cells (*62*). We observed a significant reduction in the level of Ifnα in

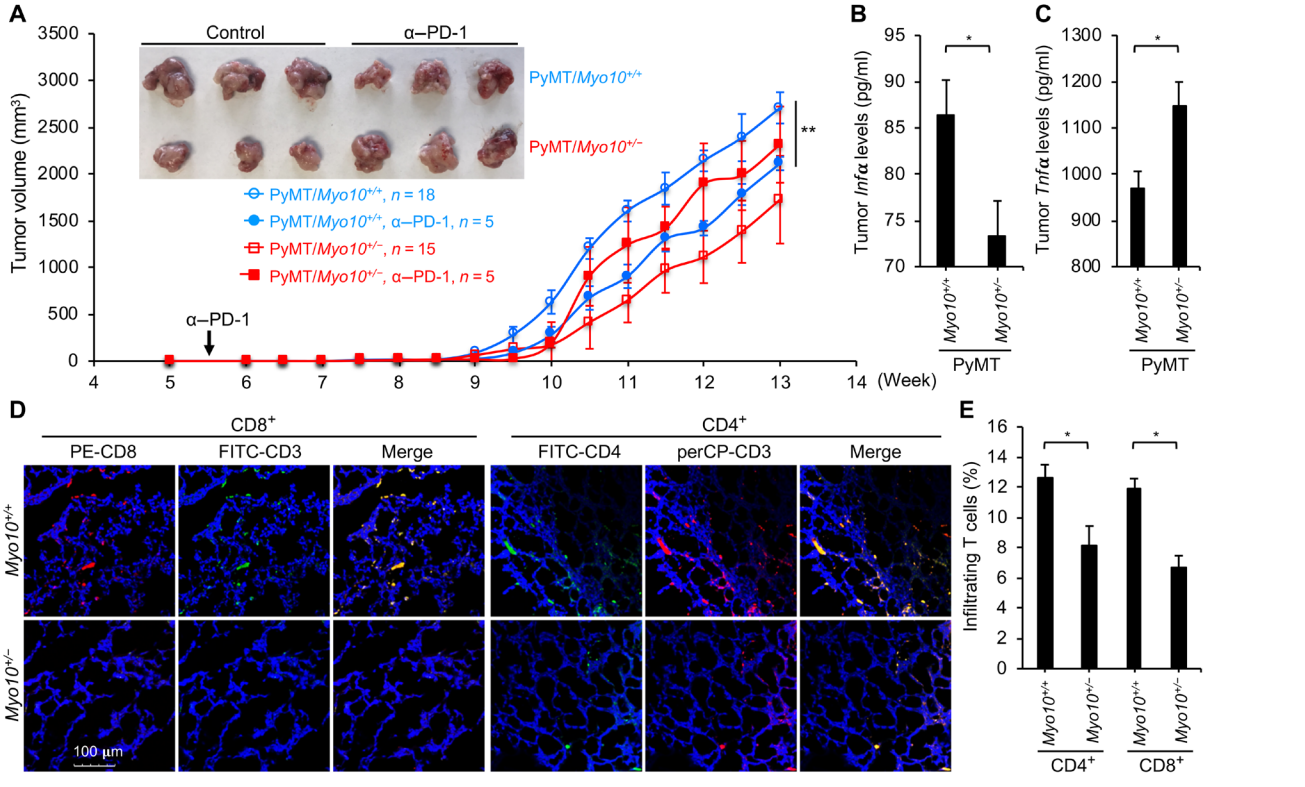

Fig. 8. MYO10 regulates tumor response to ICBs. (**A**) PyMT/*Myo10*$^{+/+}$ and PyMT/*Myo10*$^{+/-}$ mice were treated with monoclonal anti–PD-1 antibodies at week 5.5 (indicated by the arrow) by intraperitoneal injection and continued until week 13. Tumor volume was measured. Representative tumor images from three mice are shown. ELISA analysis of *Ifnα* (**B**) and *Tnfα* (**C**) in tumors from PyMT/*Myo10*$^{+/+}$ and PyMT/*Myo10*$^{+/-}$ mice. (**D**) Tumor tissues from PyMT/*Myo10*$^{+/+}$ and PyMT/*Myo10*$^{+/-}$ female mice were analyzed for infiltrating T lymphocytes. Representative images are shown. Scale bar, 100 μm. PE, phycoerythrin; FITC, fluorescein isothiocyanate. (**E**) Quantitation of percentage of tumor cells that are CD4$^+$ or CD8$^+$ in (D). Data represent average and SEM. $^{**}P < 0.001$ and $^{*}P < 0.05$.

PyMT/Myo10$^{+/-}$ tumors compared with PyMT/Myo10$^{+/+}$ tumors (Fig. 8B). On the other hand, the level of the tumor necrosis factor α (Tnfα) was significantly increased in PyMT/Myo10$^{+/-}$ tumors (Fig. 8C). While IFNα has been generally considered to be tumor suppressive (*63*), increasing evidence suggests that TNFα can suppress the tumor immune response by enhancing regulatory T lymphocytes (*64*), regulatory B lymphocytes (*65*), and myeloid-derived suppressor cells (*66*). Hence, these data support the idea that tumors from the PyMT/Myo10$^{+/-}$ mice had a reduced immunogenic microenvironment.

To further test this idea, we examined infiltrating T lymphocytes in these tumors. Our results show that tumors from the PyMT/Myo10$^{+/+}$ mice had much more infiltrating CD8^{+} and CD4^{+} T cells than in tumors from the PyMT/Myo10$^{+/-}$ mice (Fig. 8, D and E), supporting the idea that MYO10^{high} creates an immunogenic environment that responds to ICBs. In conclusion, these data suggest a potentially important role of MYO10 in cancer, revealing previously uncharacterized mechanisms by which MYO10 regulates genome stability and cancer progression.

DISCUSSION

Abnormal nuclear structures seen in cancer cells include, but are not limited to, irregular nuclear shape, fragile nucleus, and altered chromosome topology (*67*), all of which could alter the chromosome territory and ultimately lead to genomic instability. Other than defects in the nuclear structural genes, recent studies suggest that the LINC complex also affects the nuclear integrity (*5*). Here, we present a previously uncharacterized finding that a cytoplasmic protein, MYO10, regulates genome stability at least partially through mediating the LINC-nucleus network followed by mitotic regulation. Further, our studies propose a model in which MYO10^{high} or overexpression creates an inflammatory tumor microenvironment that leads to T cell exhaustion, which promotes tumor growth. Yet, in the meantime, the immunogenic potential of the tumor environment (i.e., increased genomic instability and the presence of infiltrating T cells) enhanced the tumor response to ICBs (see model in fig. S20).

We showed that the protein level of MYO10 is critical for this function. We also identified UbcH7 and β-TrCP1 as the E2 and E3 enzymes, respectively, for MYO10 ubiquitination and degradation. Because MYO10 is a motor protein that binds to and regulates the tension of the cytoskeleton and interacts with the LINC complex, elevated levels (at or above approximately twofold) of MYO10 may disrupt the proper cytoskeleton-nucleus network balance (e.g., causing abnormal perinuclear localization of Nesprin, the outer nuclear membrane portion of the LINC complex that connects to the cytoplasm), which consequently results in abnormal nuclear morphology. This aberrant nuclear morphology will likely cause abnormal mitosis to form micronuclei, exacerbating genomic instability and triggering the cGAS/STING pathway to induce transcription of inflammatory genes such as ILs and IFNs mediated at least partially through P65 nuclear translocation (fig. S20). These effects are unlikely related to the previously reported function of MYO10 in regulating filopodia, a cellular membrane structure that is involved in cell movement (*24*).

Consistent with our model, we observed greatly elevated levels of ILs and IFN response regulators in cancer cells overexpressing MYO10. On the other hand, depleting MYO10 significantly reduced the production of these inflammatory factors. Treatment with aspirin or depletion of STING to reduce inflammation significantly reduced tumor growth of both MYO10^{high} and MYO10-overexpressing breast tumors in mice. This is consistent with epidemiological studies showing that long-term users of aspirin or nonsteroidal anti-inflammatory drugs significantly reduced cancer risk (*68*).

Our data also offer some intriguing yet important insights into the role of MYO10 in determining the tumor response to ICBs. First, the fact that PyMT/*Myo10*$^{+/+}$ tumors responded to ICBs supports the idea that MYO10^{high} conferred an immunogenic environment. Second, the fact that PyMT/Myo10$^{+/-}$ mice actually grew larger in the presence of anti–PD-1 therapy suggests that reducing the level of MYO10 leads to immunotherapy resistance. Such a tumor-promoting effect (or hyperprogression) of anti–PD-1 in immune-resistant tumors is not uncommon. For instance, anti–PD-1 promoted the growth of non–small cell lung cancer–derived patient-derived xenograft models (*69*). The exact mechanisms underlying ICB's hyperprogression are poorly understood and likely context dependent. For instance, loss of programmed cell death ligand 1 (PD-L1) or Serine/Threonine kinase 11 (STK11) (*70*) or the presence of epidermal growth factor receptor mutation and MDM proto-oncogene 2/4 (MDM2/4) amplification (*71*) were reported to induce anti–PD-1 hyperprogression. The mechanisms by which PyMT/Myo10$^{+/-}$ tumors grew larger in the presence of anti–PD-1 were probably related to the altered tumor microenvironment (e.g., reduced and increased secretion of *Ifnα* and Tnfα, respectively, and less infiltrating T cells). Nonetheless, the implications of these findings are significant. Determination of tumor PD-L1 expression and/or quantification of tumor-infiltrating lymphocytes are considered to predict the response to ICBs, but their effects have been questioned (*72*, *73*). Our findings led us to propose that breast tumors with MYO10^{high} will respond to ICBs. On the other hand, they also warn us that tumors with low MYO10 might be resistant to ICBs, and therefore, the application of this type of anticancer agents should be avoided. In conclusion, our results reveal a previously uncharacterized role of MYO10 in tumor development and immune therapy response, highlighting the potential of targeting this gene in cancer.

MATERIALS AND METHODS

Cell cultures, reagents, and transfection

The human cervical cancer cell line HeLa, the osteosarcoma cancer cell line U2OS, the lung adenocarcinoma cancer cell line A549, the breast cancer cell lines (MDA-MB-231 and MCF7), diploid human embryonic lung fibroblasts WI38, human retinal pigment epithelial ARPE19, and human embryonic kidney cell line HEK293T were cultured in Dulbecco's modified Eagle's medium (DMEM) with 10% fetal bovine serum (FBS) and 1% penicillin-streptomycin. The breast cancer cell lines (HCC1143 and HCC70) were cultured in RPMI 1640 with 10% FBS and 1% penicillin-streptomycin. The breast cell lines (MCF10A and MCF10A-Neu) were cultured in DMEM/F12 with high glucose, L-glutamine, 32 mM sodium bicarbonate, cholera toxin (0.1 μg/ml), hydrocortisone (0.5 μg/ml), insulin (0.01 mg/ml), 0.05% horse serum, epidermal growth factor (0.02 μg/ml), and 1% penicillin-streptomycin. The human fetal lung fibroblast IMR-90 cells were cultured in Eagle's minimal essential medium with nonessential amino acids and 10% fetal calf serum and 1% penicillin-streptomycin. CHX was purchased from Acros Organics (New Jersey, USA). CHX was freshly dissolved in phosphate-buffered saline (PBS) before use at a concentration of 32 mM. MG132 was

purchased from Selleck Chemicals LLC (Houston, TX, USA) and dissolved in dimethyl sulfoxide at the stock concentration of 10 mM. Protein A and G beads (#SC-2003) were from Santa Cruz Biotechnology (Dallas, TX, USA). Aspirin (A2093-100G) was purchased from Sigma-Aldrich Inc. (St. Louis, MO, USA). Matrigel (#356230) was purchased from Corning (New York, USA). Cell transfection was performed with the X-tremeGENE HP transfection reagent (Sigma-Aldrich, St. Louis, MO, USA) according to the manufacturer's protocols or polyethylenimine (PEI) 300.

Antibodies

The following commercially available antibodies were used: anti-MYO10 [Santa Cruz Biotechnology, #sc-166720, or Proteintech, #24565-1-AP, for immunofluorescence staining], anti-UbcH7 (Novus, #NB100-2265), anti–lamin A/C (Santa Cruz Biotechnology, #sc-7292), anti-Nesprin3 (Abcam, #ab74261), anti-ANAPC2 (Santa Cruz Biotechnology, #sc-20984), anti-Flag M2 (Sigma-Aldrich, #F3165), anti-CHK1 (Santa Cruz Biotechnology, #sc-56291), anti-CTSL (Santa Cruz Biotechnology, #sc-32320), anti–tubulin 4A (GeneTex, #GTX112141), anti-synemin (Santa Cruz Biotechnology, #sc-374484), anti-actin (Santa Cruz Biotechnology, #sc-47778), anti-GFP (Novus, #NB100-1770, or Proteintech, #50430-2-AP), anti-Neu (Santa Cruz Biotechnology, #sc-33684), anti–glyceraldehyde phosphate dehydrogenase (Proteintech, #60004), anti-V5 (Cell Signaling Technology, #13202S), anti-p65/RELA (Bethyl Laboratories, #A301-824A), anti-STING (Cell Signaling Technology, #13647S), anti-cGAS (Cell Signaling Technology, #15102S), anti-pSTAT1 (Cell Signaling Technology, #9167S), anti-pSTAT3 (Cell Signaling Technology, #9131S), anti–IL-1β (NCI-monoclonal 3ZD), anti–IL-8 (Santa Cruz Biotechnology, #sc-376750), anti-pTBK1 (Cell Signaling Technology, #5483S), anti-pIRF3 (Cell Signaling Technology, #29047S), and anti–phospho-histone H3 (Ser^{10}) (Millipore, #06-570). Rat anti-mouse CD279 (PD-1, #P362) was purchased from Leinco Technologies Inc. (St. Louis, MO, USA). Rat anti-mouse phycoerythrin (PE)–CD8α (#553033), hamster anti-mouse peridinin-chlorophyll-protein (PerCP)–CD3e (#553067), rat anti-mouse fluorescein isothiocyanate (FITC)–CD4 (#553729), and hamster anti-mouse FITC-CD3e (#553062) were from DB Pharmingen (San Jose, CA, USA). The goat anti-mouse (#PI-31430) and goat anti-rabbit (#PI-31460) horseradish peroxidase (HRP)–conjugated antibodies were purchased from Pierce/Thermo Fisher Scientific. The anti-goat HRP-conjugated antibody was purchased from Invitrogen (USA). Alexa Fluor 488 goat anti-mouse immunoglobulin G (IgG) (H + L), Alexa Fluor 488 goat anti-rabbit IgG (H + L), Alexa Fluor 594 goat anti-mouse IgG (H + L), and Alexa Fluor 594 goat anti-rabbit IgG (H + L) were obtained from Life Technologies/Thermo Fisher Scientific.

RNA interference

For RNAi, lentiviral shRNA vectors targeting UbcH7, CTSL, lamin A/C, and MYO10 were obtained from Sigma-Aldrich (St. Louis, MO, USA). The following are targeting sequences for UbcH7: CCAGCAGAGTACCCATTCAAA (TRCN0000007209) and CCACCGAAGATCACATTTAAA (TRCN0000007211); CTSL: CCAAAGACCGGAGAAACCATT (TRCN0000349635) and AGGCGATGCACAACAGATTAT (TRCN0000318682); lamin A/C: GATGATCCCTTGCTGACTTAC (TRCN0000262697) and AGAAGGAGGGTGACCTGATAG (TRCN0000262764); and MYO10: ACTAACCTCCCAACCTGATTT (TRCN0000298630) and GATAGGACTTTCCACCTGATT (TRCN0000123088). siRNA duplexes targeting β-TrCP1 were purchased from GE Healthcare/Dharmacon (Lafayette, CO, USA).

For lentivirus production, we followed procedures that we previously described (*33*). Briefly, we cultured HEK293T cells in 10-cm dishes at ~50% confluency the day before transfection. We prepared the transfection complex as follows: 12 μg of DNA (3 μg of shRNA, 3 μg of pGag/pol, 3 μg of pVSV-G, and 3 μg of pRSV-Rev) in 250 μl of sterile ultrapure H_2O containing 62 μl of 2 M $CaCl_2$. The mixture was incubated at room temperature for 5 min, was added 250 μl of 2× Hanks' balanced salt solution buffer and incubated for another 20 min, and was added dropwise to preplated HEK293T cells. After 72 hours, the culture media were collected and centrifuged at 2000 rpm for 10 min at 4°C, and the supernatant was transferred to a new tube to infect cells or stored at 4°C. Target cells were seeded 1 day before transduction. The culture medium of target cells was aspirated, replaced with fresh complete media and virus-containing supernatant at a 1:1 (v/v) ratio with polybrene (4 to 10 μg/ml). The cells were cultured for 2 to 3 days, and stable clones were obtained by selecting cells with puromycin (3 μg/ml) for 2 weeks.

Western blot analysis

For protein expression analysis, cultured cells or digested tissues were extracted by the NP-40 lysis buffer [50 mM tris-HCl (pH 7.6), 150 mM NaCl, 10 mM NaF, and 0.5% Nonidet P-40] supplemented with 1 mM phenylmethylsulfonyl fluoride (PMSF), 1 mM dithiothreitol (DTT), aprotinin (10 μg/ml), and leupeptin (1 μg/ml). Lysis was performed for 30 min on ice followed by sonication for 10 s two times. Protein concentrations were determined by the bicinchoninic acid assay (BCA) method (Pierce BCA Protein Assay, Thermo Fisher Scientific, USA). The amount of 100 μg of total proteins was separated on gradient SDS–polyacrylamide gel electrophoresis (SDS-PAGE) gels, transferred to polyvinylidene difluoride membrane (Immobilon, Millipore, Bedford, MA), and blotted with specific antibodies (1:1000 dilution for all antibodies unless specifically indicated).

Immunoprecipitation

For endogenous protein IP, at least 2×10^6 cells were lysed in 1 ml of NP40 lysis buffer on ice for 30 min and then were briefly sonicated (2% power output, 5 s per cycle for 2 cycles). The cell lysates were centrifuged at 13,000 rpm for 10 min at 4°C, and the supernatants were incubated with primary antibodies (1 μg/1 mg of lysates) overnight at 4°C. Then, Protein A and G agarose beads (50 μl of slurry) were added into each sample and further incubated for 2 hours, washed four times with lysis buffer, and collected by centrifuge at 13,000 rpm for 1 min, and the beads were boiled with 40 μl of 2× sample buffer before running on SDS-PAGE.

To immunoprecipitate exogenously expressed proteins, HEK293T cells were transfected with specific plasmids by PEI300 (1 μg of DNA per 3 μl of PEI) for 48 hours, treated or not before cell lysis. For HEK293T cells, greater than 50% transfection efficiency was achieved by this method of transfection. The clear cell lysates were incubated with the primary antibody of FLAG-M2 (Sigma-Aldrich) or GFP (Novus or Proteintech) overnight at 4°C. Then, the samples were processed as stated above.

Immunofluorescence of cell cultures

To prepare slides for immunofluorescence staining, cells were plated on glass coverslips in six-well plates and allowed to grow for 24 hours.

Cells were then transfected or treated as indicated in specific experimental settings, fixed in 4% paraformaldehyde in PBS for 10 min at room temperature, followed by washing with PBS three times. Cells were permeabilized with 0.5% Triton X-100 in PBS for 10 min and incubated in blocking buffer [10% FBS, 0.5% bovine serum albumin (BSA), and 0.2% Triton X-100 in PBS] at room temperature for 30 min. Cells were washed four times with 0.2% Triton X-100 in PBS for 5 min and incubated in 0.2% Triton X-100 in PBS containing primary antibodies (1:30 to 1:500 dilution) for overnight at 4°C. The slides were washed with 0.2% Triton X-100 in PBS four times, and secondary antibodies conjugated with Alexa Fluor 488 or Alexa Fluor 594 were added at 1:1000 dilution on cover glasses and incubated for 1 hour in the dark at room temperature. The samples were mounted with ProLong Gold Antifade solution containing 4′,6-diamidino-2-phenylindole (DAPI) (#P36931, Life Technologies/Thermo Fisher Scientific, Carlsbad, CA, USA) and visualized under a fluorescence microscope.

Cell fractionation

Cells cultured in a 6-cm dish were washed with PBS twice; lysed in 150 μl of lysis buffer [10 mM Hepes (pH 7.9), 1.5 mM $MgCl_2$, 10 mM KCl, 0.43 M sucrose, 10% glycerol, and 0.1% Triton X-100] supplemented with 1 mM PMSF, 1 mM DTT, aprotinin (10 μg/ml), leupeptin (1 μg/ml); and incubated on ice for 5 min. The cell lysate was then subjected to centrifugation at 2000 rpm for 5 min at 4°C. The supernatant was collected as cytoplasmic proteins. The pellet was washed with ice-cold PBS and lysed in 150 μl of NP40 buffer. After 10 min of incubation on ice, the samples were sonicated for 10 s two times to complete cell lysis, and the lysate was centrifuged at 12,000 rpm for 10 min, which mainly contains the nuclear extract.

Metaphase spreading and chromosome counting

HCC1143 parental or V5-MYO10–expressing cells were treated with colchicine (0.5 μg/ml) for 2 hours at 37°C, collected into a 15-ml tube, and centrifuged at 1200 rpm for 10 min. The cell pellet was gently washed two times with PBS and resuspended in hypotonic solution (0.075 M KCl) and allowed to stand for 30 min at room temperature. Cells were fixed in methanol:acetic acid [3:1 (v/v)] for 5 min at room temperature. The suspension was then dropped onto glass slides and dried at 37°C. The samples were subjected to DAPI staining and visualized under a fluorescence microscope.

SILAC assay

To prepare for SILAC analysis, A549 control or shUbcH7 stable cells were grown in SILAC medium (Thermo Fisher Scientific, #PI89985) with 10% dialyzed SILAC FBS (Thermo Fisher Scientific, # PI88440) and supplemented with either light or heavy isotope-labeled amino acids. Control cells were cultured with regular media containing ^{12}C-Leu/^{12}C-Arg, whereas shUbcH7 group cells were cultured with ^{13}C-Leu (Thermo Fisher Scientific, #PI88435) and ^{13}C-Arg (Thermo Fisher Scientific, #PI88210) media. Cells were passaged every 2 to 3 days for 10 passages, during which SILAC-grade PBS (Thermo Fisher Scientific, #1315014) and collagenase (Thermo Fisher Scientific, #17104019) were used. Subsequently, light and heavy amino acid–labeled cells were collected, lysed in SILAC-grade radioimmunoprecipitation assay buffer (Thermo Fisher Scientific, #PI89900) on ice for 20 min, sonicated, and centrifuged, and the supernatant was collected. The protein lysates were quantitated by a Pierce BCA protein assay kit (Thermo Fisher Scientific, #PI23225, Franklin, MA, USA), and equal amounts of cell lysates from control and shUbcH7 groups were mixed (1:1 ratio) and run on 10% SDS-PAGE. The gel was silver-stained and excised into 10 slices and submitted for mass spectrometry analysis.

Protein sequence analysis by liquid chromatography–tandem mass spectrometry

Gel slices were further cut into ~1-mm^3 pieces, dehydrated with acetonitrile for 10 min, washed off acetonitrile, completely dried in a SpeedVac, and stored for processing. Rehydration of the gel was done in 50 mM ammonium bicarbonate containing trypsin (12.5 ng/μl) (Promega, Madison, WI) at 4°C for 45 min and then incubated the sample at 37°C overnight. Ammonium bicarbonate was removed from the digestion products, washed the sample with solution containing 50% acetonitrile and 1% formic acid once, dried, and stored at 4°C until analysis. The samples were run on an LTQ Orbitrap Velos Pro ion-trap mass spectrometer (Thermo Fisher Scientific, Waltham, MA). Peptide identification was determined by matching the protein database with fragmentation signatures, and data were filtered by a 1 to 2% peptide false discovery rate.

Quantitative polymerase chain reaction

We performed quantitative polymerase chain reaction (qPCR) according to the Minimum Information for Publication of Quantitative Real-Time PCR Experiments (MIQE) guidelines. Briefly, total RNA was extracted from HCC70 parental or MYO10-depleted cells by TRIzol (#15596026, Thermo Fisher Scientific, Waltham, MA, USA). The complementary DNA (cDNA) synthesis was conducted by the RevertAid first-strand cDNA synthesis kit (#K1622, Thermo Fisher Scientific). qPCR was run on a CFX96 real-time PCR system (Bio-Rad, Hercules, CA, USA) using the SYBR Green Master Mix (#208054, Invitrogen/Thermo Fisher Scientific, Franklin, MA, USA). The gene expression level was determined by analyzing $2\text{-}\Delta\Delta C_t$ using actin as the control. The qPCR program is as follows: 95°C for 3 min, 95°C for 10 s for 40 cycles, and then 60°C for 30 s. Following the qPCR cycle, the melt curve was determined by heating the samples to 95°C for 10 s, reducing to 60°C for 30 s, and then gradually increasing to 95°C with 0.5°C increment increases.

Primers sequences for human target genes are as follows: IL-1β forward: 5′-ACCTGAGCTCGCCAGTGAA-3′ and IL-1β reverse: 5′-TCGGAGATTCGTAGCTGGAT-3′; IFNB1 forward: 5′-TGTCGCCTACTACCTGTTGTGC-3′ and IFNB1 reverse: 5′-AACTGCAACCTTTCGAAGCC-3′; TNFα forward: 5′-TCTCTCAGCTCCACGCCATT-3′ and TNFα reverse: 5′-CCCAGGCAGTCAGATCATCTTC-3′; CDKN1A forward: 5′-AACTAGGCGGTTGAATGAGAG-3′ and CDKN1A reverse: 5′-GAGGAAGTAGCTGGCATGAAG-3′; and β-actin forward: 5'-GTCCCTCACCCTCCCAAAAGC-3′ and β-actin reverse: 5'-GCTGCCTCAACACCTCAACCC-3′.

Tumor mouse xenografts

A total of 4.5×10^6 HCC1143 parental, MYO10-depleted, V5-MYO10–overexpressing, and V5-MYO10–overexpressing but STING stably depleted cells suspended in Matrigel at a 1:1 ratio were implanted into the mammary fat pad of 8-week-old female nude or NOD-SCID mice purchased from the Jackson Laboratory (Bar Harbor, ME, USA). All mice studies were approved by the Institutional Animal Care and Use Committee at Case Western Reserve University (CWRU) and are consistent with the recommendations of the American

Veterinary Medical Association Guidelines on Euthanasia before the initiation of experiments. All mice were housed in-group in cages with bedding, controlled temperature (23° ± 2°C), humidity (50 ± 5%), and illumination (12-hour light/12-hour dark cycle). Mice were adapted to the facility for 1 week before experiments. Tumor volumes were measured every 2 days using a caliper and determined by a formula [volume = (length × width^2)/2] starting from day 5 after implantation. The results were expressed as mean tumor volumes with SD. Aspirin (100 mg/kg) dissolved in PBS was administered orally daily using oral gavage tube starting from day 5 after tumor implantation.

Generation of *MYO10*$^{+/-}$ cells

MYO10 knockout U2OS or MDA-MB-2312 cells were generated by CRISPR-Cas9 as previously described with modifications (*74*). Briefly, a 22–base pair oligonucleotide targeting the PEST domain of MYO10 (TAGGTGGACTCGCCGCTGGAGG) was identified using the MIT CRISPR design tool. The annealed double-strand oligo was ligated to the pSpCas9(BB)-2A-Puro (PX459) vector (Addgene, #48139). U2OS or MDA-MB-231 cells were transfected with the targeting plasmid using Lipofectamine. After puromycin selection of transfected cells by 2 days, cells were replated into dishes at nearly single-cell density. After ~2 weeks, visible single colonies were picked up and cultured in 24-well plates. Expression of MYO10 protein was examined by Western blotting using a mouse monoclonal anti-MYO10 antibody. MYO10 gene deletion was confirmed by genomic DNA sequencing.

Knockout and transgenic mice

Rederivation of *Myo10*^{tm1d} mice in the C57BL/6J background was performed at the CWRU Transgenic and Targeting facility. Two *Myo10*$^{+/-}$ founder male mice were confirmed by genotyping and were crossed with WT female FVB/NJ mice to produce pups. The resultant *Myo10*$^{+/-}$ male mice were crossed with WT FVB/NJ female mice, and this process was repeated six times to obtain heterozygous mice (both male and female) with the FVB/N genetic background. The sixth-generation *Myo10*$^{+/-}$ female mice were then crossed with MMTV-PyMT male mice purchased from the Jackson Laboratory to obtain PyMT/*Myo10*$^{+/+}$, PyMT/*Myo10*$^{+/-}$, and PyMT/*Myo10*$^{-/-}$ mice. Mice genotyping was performed according to the Jackson Laboratory for PyMT or as previously reported for *Myo10* (*35*). Mice were examined twice a week in the mammary glands to detect tumor development.

Treatment with anti–PD-1 antibodies

Starting from week 5.5 of age, MMTV-PyMT/*Myo10*$^{+/+}$ and MMTV-PyMT/*Myo10*$^{+/-}$ female mice (five per group) were given the monoclonal anti–PD-1 antibody (150 μg) by intraperitoneal injection every 4 days and continued until the age of 13 weeks. Tumor volumes were analyzed as stated above. The animals were euthanized at approximately week 10 of age, and tumors were taken for analyses of cytokines and the presence of infiltrating T lymphocytes.

Enzyme-linked immunosorbent assay analysis in cell cultures and tumor tissues

The levels of *Ifn*α (MyBioSource, #MBS2506010) and *Tnf*α (RayBiotech, #ELM-TNFa-1) in tumors from MMTV-PyMT/*Myo10*$^{+/+}$ and MMTV-PyMT/*Myo10*$^{+/-}$ female mice were measured by enzyme-linked immunosorbent assay (ELISA). Briefly, xenografted tumors from approximately week 10 of mice were surgically removed, and approximately 100 mg of tumor tissues was dissected on ice into small pieces and added ~300 μl of lysis buffer [100 mM tris (pH 7.4), 150 mM NaCl, 1 mM EGTA, 1 mM EDTA, 0.5% NP40, and 0.5% sodium deoxycholate]. Tissues were homogenized on ice for 30 to 60 s followed by sonication for 10 s and centrifuged at 10,000 rpm for 20 min at 4°C, and the supernatant was collected for ELISA analysis.

To measure cGAMP (Cayman, #501700) in cultured cells, HCC1143 (parental, MYO10 depleted, V5-MYO10 overexpressing, and V5-MYO10 overexpressing but STING depleted) or HCC70 (parental and MYO10 depleted) cells were collected, lysed in extraction buffer with vortex, and centrifuged at 13,000 rpm for 10 min at 4°C, and the supernatants were collected for analysis. ELISA was performed according to the manufacturer's instructions. The absorbance was normalized by protein content in each group, and the levels of cGAMP, Ifnα, and Tnfα were determined by the standard curve. Data were acquired from three replicates.

Tumor tissue immunofluorescence staining

Tumor tissue samples were established from spontaneous mammary tumors arising in MMTV-PyMT and MMTV-PyMT/*Myo10*$^{+/-}$ female mice. In a small container, a fresh tissue sample was carefully coated with optimal cutting temperature (OCT) compound at room temperature. OCT-coated samples were placed into an appropriately sized cryomold and covered the tissue with OCT. Forceps were used to lower the embedded tissues into the isopentane without fully submerging, keeping the cryomold in contact with isopentane until the OCT has solidified and turned white. Once frozen, the cryomold was placed on powdered dry ice, and frozen embedded tissues were stored at −80°C. For all tumor samples, 5-μm tissue sections were cut using a Leica CM1850 cryostat microtome, and samples were mounted on glass microscope slides and left to air-dry for 2 hours at room temperature. The samples were fixed with methanol at 20°C for 15 min and then air-dried for 30 min. Samples were blocked with blocking buffer (PBS/1% FBS /0.5% BSA/0.1% Triton X-100) and then added conjugated primary antibodies (rat anti-mouse PE-CD4, hamster anti-mouse PerCP-CD3e, rat anti-mouse FITC-CD4, and rat anti-mouse FITC-CD3e; 1:1000 diluted in 0.5% BSA/PBS) and incubated at 4°C overnight while avoiding drying. The slides were washed five times with 0.1% Triton X-100 in PBS for 5 min each, mounted in 200 μl of DAPI (final concentration of 1 μg/ml, 1:1000 dilute in PBS) for 5 min, washed with PBS three times, and visualized under a confocal microscope.

Statistical analysis

All cell culture experiments were performed at least twice. Data are presented as means ± SD (or SEM unless indicated otherwise). The statistical analysis was conducted by the Prism 8.0 (GraphPad) software. Pairwise comparison was performed using a two-tailed Student's *t* test, whereas one-way analysis of variance (ANOVA) was used to compare multiple comparisons. *P* values of less than at least 0.05 were considered statistically significant.

SUPPLEMENTARY MATERIALS

Supplementary material for this article is available at https://science.org/doi/10.1126/sciadv.abg6908

View/request a protocol for this paper from *Bio-protocol*.

REFERENCES AND NOTES

1. L. Pikor, K. Thu, E. Vucic, W. Lam, The detection and implication of genome instability in cancer. *Cancer Metastasis Rev.* **32**, 341–352 (2013).
2. C. R. Boland, A. Goel, Microsatellite instability in colorectal cancer. *Gastroenterology* **138**, 2073–2087.e3 (2010).
3. S. L. Carter, A. C. Eklund, I. S. Kohane, L. N. Harris, Z. Szallasi, A signature of chromosomal instability inferred from gene expression profiles predicts clinical outcome in multiple human cancers. *Nat. Genet.* **38**, 1043–1048 (2006).
4. S. P. Jackson, J. Bartek, The DNA-damage response in human biology and disease. *Nature* **461**, 1071–1078 (2009).
5. T. J. Kirby, J. Lammerding, Emerging views of the nucleus as a cellular mechanosensor. *Nat. Cell Biol.* **20**, 373–381 (2018).
6. M. Crisp, Q. Liu, K. Roux, J. B. Rattner, C. Shanahan, B. Burke, P. D. Stahl, D. Hodzic, Coupling of the nucleus and cytoplasm: Role of the LINC complex. *J. Cell Biol.* **172**, 41–53 (2006).
7. D. A. Starr, H. N. Fridolfsson, Interactions between nuclei and the cytoskeleton are mediated by SUN-KASH nuclear-envelope bridges. *Annu. Rev. Cell Dev. Biol.* **26**, 421–444 (2010).
8. D. Rajgor, C. M. Shanahan, Nesprins: From the nuclear envelope and beyond. *Expert Rev. Mol. Med.* **15**, e5 (2013).
9. F. Lottersberger, R. A. Karssemeijer, N. Dimitrova, T. de Lange, 53BP1 and the LINC complex promote microtubule-dependent DSB mobility and DNA repair. *Cell* **163**, 880–893 (2015).
10. R. K. Swartz, E. C. Rodriguez, M. C. King, A role for nuclear envelope-bridging complexes in homology-directed repair. *Mol. Biol. Cell* **25**, 2461–2471 (2014).
11. K. S. Lawrence, E. C. Tapley, V. E. Cruz, Q. Li, K. Aung, K. C. Hart, T. U. Schwartz, D. A. Starr, J. Engebrecht, LINC complexes promote homologous recombination in part through inhibition of nonhomologous end joining. *J. Cell Biol.* **215**, 801–821 (2016).
12. T. Li, Z. J. Chen, The cGAS-cGAMP-STING pathway connects DNA damage to inflammation, senescence, and cancer. *J. Exp. Med.* **215**, 1287–1299 (2018).
13. S. M. Harding, J. L. Benci, J. Irianto, D. E. Discher, A. J. Minn, R. A. Greenberg, Mitotic progression following DNA damage enables pattern recognition within micronuclei. *Nature* **548**, 466–470 (2017).
14. K. J. Mackenzie, P. Carroll, C. A. Martin, O. Murina, A. Fluteau, D. J. Simpson, N. Olova, H. Sutcliffe, J. K. Rainger, A. Leitch, R. T. Osborn, A. P. Wheeler, M. Nowotny, N. Gilbert, T. Chandra, M. A. M. Reijns, A. P. Jackson, cGAS surveillance of micronuclei links genome instability to innate immunity. *Nature* **548**, 461–465 (2017).
15. C. Zierhut, N. Yamaguchi, M. Paredes, J. D. Luo, T. Carroll, H. Funabiki, The cytoplasmic DNA sensor cGAS promotes mitotic cell death. *Cell* **178**, 302–315.e23 (2019).
16. B. Guey, M. Wischnewski, A. Decout, K. Makasheva, M. Kaynak, M. S. Sakar, B. Fierz, A. Ablasser, BAF restricts cGAS on nuclear DNA to prevent innate immune activation. *Science* **369**, 823–828 (2020).
17. L. Mohr, E. Toufektchan, P. von Morgen, K. Chu, A. Kapoor, J. Maciejowski, ER-directed TREX1 limits cGAS activation at micronuclei. *Mol. Cell* **81**, 724–738.e9 (2021).
18. S. F. Bakhoum, B. Ngo, A. M. Laughney, J. A. Cavallo, C. J. Murphy, P. Ly, P. Shah, R. K. Sriram, T. B. K. Watkins, N. K. Taunk, M. Duran, C. Pauli, C. Shaw, K. Chadalavada, V. K. Rajasekhar, G. Genovese, S. Venkatesan, N. J. Birkbak, N. McGranahan, M. Lundquist, Q. LaPlant, J. H. Healey, O. Elemento, C. H. Chung, N. Y. Lee, M. Imielenski, G. Nanjangud, D. Pe'er, D. W. Cleveland, S. N. Powell, J. Lammerding, C. Swanton, L. C. Cantley, Chromosomal instability drives metastasis through a cytosolic DNA response. *Nature* **553**, 467–472 (2018).
19. F. Odronitz, M. Kollmar, Drawing the tree of eukaryotic life based on the analysis of 2,269 manually annotated myosins from 328 species. *Genome Biol.* **8**, R196 (2007).
20. D. S. Courson, R. E. Cheney, Myosin-X and disease. *Exp. Cell Res.* **334**, 10–15 (2015).
21. J. S. Berg, B. H. Derfler, C. M. Pennisi, D. P. Corey, R. E. Cheney, Myosin-X, a novel myosin with pleckstrin homology domains, associates with regions of dynamic actin. *J. Cell Sci.* **113** (Pt. 19), 3439–3451 (2000).
22. J. S. Berg, R. E. Cheney, Myosin-X is an unconventional myosin that undergoes intrafilopodial motility. *Nat. Cell Biol.* **4**, 246–250 (2002).
23. H. Tokuo, Myosin X. *Adv. Exp. Med. Biol.* **1239**, 391–403 (2020).
24. P. K. Mattila, P. Lappalainen, Filopodia: Molecular architecture and cellular functions. *Nat. Rev. Mol. Cell Biol.* **9**, 446–454 (2008).
25. G. Jacquemet, H. Hamidi, J. Ivaska, Filopodia in cell adhesion, 3D migration and cancer cell invasion. *Curr. Opin. Cell Biol.* **36**, 23–31 (2015).
26. R. Cao, J. Chen, X. Zhang, Y. Zhai, X. Qing, W. Xing, L. Zhang, Y. S. Malik, H. Yu, X. Zhu, Elevated expression of myosin X in tumours contributes to breast cancer aggressiveness and metastasis. *Br. J. Cancer* **111**, 539–550 (2014).
27. M. E. Ross, X. Zhou, G. Song, S. A. Shurtleff, K. Girtman, W. K. Williams, H. C. Liu, R. Mahfouz, S. C. Raimondi, N. Lenny, A. Patel, J. R. Downing, Classification of pediatric acute lymphoblastic leukemia by gene expression profiling. *Blood* **102**, 2951–2959 (2003).
28. Y. Sun, X. Ai, S. Shen, S. Lu, NF-κB-mediated miR-124 suppresses metastasis of non-small-cell lung cancer by targeting MYO10. *Oncotarget* **6**, 8244–8254 (2015).
29. H. Tokuo, J. Bhawan, L. M. Coluccio, Myosin X is required for efficient melanoblast migration and melanoma initiation and metastasis. *Sci. Rep.* **8**, 10449 (2018).
30. A. Arjonen, R. Kaukonen, E. Mattila, P. Rouhi, G. Hognas, H. Sihto, B. W. Miller, J. P. Morton, E. Bucher, P. Taimen, R. Virtakoivu, Y. Cao, O. J. Sansom, H. Joensuu, J. Ivaska, Mutant p53-associated myosin-X upregulation promotes breast cancer invasion and metastasis. *J. Clin. Invest.* **124**, 1069–1082 (2014).
31. I. A. Voutsadakis, Ubiquitin- and ubiquitin-like proteins-conjugating enzymes (E2s) in breast cancer. *Mol. Biol. Rep.* **40**, 2019–2034 (2013).
32. X. Han, L. Zhang, J. Chung, F. Mayca Pozo, A. Tran, D. D. Seachrist, J. W. Jacobberger, R. A. Keri, H. Gilmore, Y. Zhang, UbcH7 regulates 53BP1 stability and DSB repair. *Proc. Natl. Acad. Sci. U.S.A.* **111**, 17456–17461 (2014).
33. F. Mayca Pozo, J. Tang, K. W. Bonk, R. A. Keri, X. Yao, Y. Zhang, Regulatory cross-talk determines the cellular levels of 53BP1 protein, a critical factor in DNA repair. *J. Biol. Chem.* **292**, 5992–6003 (2017).
34. E. A. Whitcomb, E. J. Dudek, Q. Liu, A. Taylor, Novel control of S phase of the cell cycle by ubiquitin-conjugating enzyme H7. *Mol. Biol. Cell* **20**, 1–9 (2009).
35. E. G. Heimsath Jr., Y. I. Yim, M. Mustapha, J. A. Hammer, R. E. Cheney, Myosin-X knockout is semi-lethal and demonstrates that myosin-X functions in neural tube closure, pigmentation, hyaloid vasculature regression, and filopodia formation. *Sci. Rep.* **7**, 17354 (2017).
36. E. Coyaud, M. Mis, E. M. Laurent, W. H. Dunham, A. L. Couzens, M. Robitaille, A. C. Gingras, S. Angers, B. Raught, BioID-based identification of Skp Cullin F-box (SCF)$^{\beta\text{-TrCP1/2}}$ E3 ligase substrates. *Mol. Cell. Proteomics* **14**, 1781–1795 (2015).
37. M. E. Sowa, E. J. Bennett, S. P. Gygi, J. W. Harper, Defining the human deubiquitinating enzyme interaction landscape. *Cell* **138**, 389–403 (2009).
38. T. Y. Low, M. Peng, R. Magliozzi, S. Mohammed, D. Guardavaccaro, A. J. R. Heck, A systems-wide screen identifies substrates of the SCF$^{\beta TrCP}$ ubiquitin ligase. *Sci. Signal.* **7**, rs8 (2014).
39. J. R. Skaar, J. K. Pagan, M. Pagano, Mechanisms and function of substrate recruitment by F-box proteins. *Nat. Rev. Mol. Cell Biol.* **14**, 369–381 (2013).
40. Z. Wang, P. Liu, H. Inuzuka, W. Wei, Roles of F-box proteins in cancer. *Nat. Rev. Cancer* **14**, 233–247 (2014).
41. E. Latres, D. S. Chiaur, M. Pagano, The human F box protein β-Trcp associates with the Cul1/Skp1 complex and regulates the stability of β-catenin. *Oncogene* **18**, 849–854 (1999).
42. D. Guardavaccaro, Y. Kudo, J. Boulaire, M. Barchi, L. Busino, M. Donzelli, F. Margottin-Goguet, P. K. Jackson, L. Yamasaki, M. Pagano, Control of meiotic and mitotic progression by the F box protein β-Trcp1 in vivo. *Dev. Cell* **4**, 799–812 (2003).
43. R. D. Goldman, Y. Gruenbaum, R. D. Moir, D. K. Shumaker, T. P. Spann, Nuclear lamins: Building blocks of nuclear architecture. *Genes Dev.* **16**, 533–547 (2002).
44. J. L. Broers, F. C. Ramaekers, G. Bonne, R. B. Yaou, C. J. Hutchison, Nuclear lamins: Laminopathies and their role in premature ageing. *Physiol. Rev.* **86**, 967–1008 (2006).
45. V. Andres, J. M. Gonzalez, Role of A-type lamins in signaling, transcription, and chromatin organization. *J. Cell Biol.* **187**, 945–957 (2009).
46. T. A. Dittmer, T. Misteli, The lamin protein family. *Genome Biol.* **12**, 222 (2011).
47. Y. Cai, R. Nogales-Cadenas, Q. Zhang, J. R. Lin, W. Zhang, K. O'Brien, C. Montagna, Z. D. Zhang, Transcriptomic dynamics of breast cancer progression in the MMTV-PyMT mouse model. *BMC Genomics* **18**, 185 (2017).
48. P. J. Stephens, C. D. Greenman, B. Fu, F. Yang, G. R. Bignell, L. J. Mudie, E. D. Pleasance, K. W. Lau, D. Beare, L. A. Stebbings, S. McLaren, M. L. Lin, D. J. McBride, I. Varela, S. Nik-Zainal, C. Leroy, M. Jia, A. Menzies, A. P. Butler, J. W. Teague, M. A. Quail, J. Burton, H. Swerdlow, N. P. Carter, L. A. Morsberger, C. Iacobuzio-Donahue, G. A. Follows, A. R. Green, A. M. Flanagan, M. R. Stratton, P. A. Futreal, P. J. Campbell, Massive genomic rearrangement acquired in a single catastrophic event during cancer development. *Cell* **144**, 27–40 (2011).
49. C. L. Fonseca, H. L. H. Malaby, L. A. Sepaniac, W. Martin, C. Byers, A. Czechanski, D. Messinger, M. Tang, R. Ohi, L. G. Reinholdt, J. Stumpff, Mitotic chromosome alignment ensures mitotic fidelity by promoting interchromosomal compaction during anaphase. *J. Cell Biol.* **218**, 1148–1163 (2019).
50. K. A. Fitzgerald, S. M. McWhirter, K. L. Faia, D. C. Rowe, E. Latz, D. T. Golenbock, A. J. Coyle, S. M. Liao, T. Maniatis, IKKε and TBK1 are essential components of the IRF3 signaling pathway. *Nat. Immunol.* **4**, 491–496 (2003).
51. M. S. Hayden, S. Ghosh, Signaling to NF-κB. *Genes Dev.* **18**, 2195–2224 (2004).
52. R. Amann, B. A. Peskar, Anti-inflammatory effects of aspirin and sodium salicylate. *Eur. J. Pharmacol.* **447**, 1–9 (2002).
53. J. Dai, Y. J. Huang, X. He, M. Zhao, X. Wang, Z. S. Liu, W. Xue, H. Cai, X. Y. Zhan, S. Y. Huang, K. He, H. Wang, N. Wang, Z. Sang, T. Li, Q. Y. Han, J. Mao, X. Diao, N. Song, Y. Chen, W. H. Li, J. H. Man, A. L. Li, T. Zhou, Z. G. Liu, X. M. Zhang, T. Li, Acetylation blocks cGAS activity and inhibits self-DNA-induced autoimmunity. *Cell* **176**, 1447–1460.e14 (2019).
54. C. T. Guy, R. D. Cardiff, W. J. Muller, Induction of mammary tumors by expression of polyomavirus middle T oncogene: A transgenic mouse model for metastatic disease. *Mol. Cell. Biol.* **12**, 954–961 (1992).

55. C. T. Guy, S. K. Muthuswamy, R. D. Cardiff, P. Soriano, W. J. Muller, Activation of the c-Src tyrosine kinase is required for the induction of mammary tumors in transgenic mice. *Genes Dev.* **8**, 23–32 (1994).
56. R. S. Cook, J. T. Garrett, V. Sanchez, J. C. Stanford, C. Young, A. Chakrabarty, C. Rinehart, Y. Zhang, Y. Wu, L. Greenberger, I. D. Horak, C. L. Arteaga, ErbB3 ablation impairs PI3K/Akt-dependent mammary tumorigenesis. *Cancer Res.* **71**, 3941–3951 (2011).
57. H. Lahlou, V. Sanguin-Gendreau, D. Zuo, R. D. Cardiff, G. W. McLean, M. C. Frame, W. J. Muller, Mammary epithelial-specific disruption of the focal adhesion kinase blocks mammary tumor progression. *Proc. Natl. Acad. Sci. U.S.A.* **104**, 20302–20307 (2007).
58. R. S. Kenchappa, P. Mistriotis, E. Wisniewski, S. Bhattacharya, T. Kulkarni, R. West, A. Luu, M. Conlon, E. Heimsath, J. F. Crish, H. S. Picariello, A. Dovas, N. Zarco, M. Lara-Velazquez, A. Quinones-Hinojosa, J. A. Hammer, D. Mukhopadhyay, R. E. Cheney, K. Konstantopoulos, P. Canoll, S. S. Rosenfeld, Myosin 10 regulates invasion, mitosis, and metabolic signaling in glioblastoma. *iScience* **23**, 101802 (2020).
59. S. F. Bakhoum, L. C. Cantley, The multifaceted role of chromosomal instability in cancer and its microenvironment. *Cell* **174**, 1347–1360 (2018).
60. M. García-Aranda, M. Redondo, Immunotherapy: A challenge of breast cancer treatment. *Cancers* **11**, 1822 (2019).
61. J. C. Radosa, L. Stotz, C. Müller, A. C. Kaya, E.-F. Solomayer, M. P. Radosa, Clinical data on immunotherapy in breast cancer. *Breast Care* **15**, 450–469 (2020).
62. M. Haji Abdolvahab, M. R. K. Mofrad, H. Schellekens, Interferon beta: From molecular level to therapeutic effects. *Int. Rev. Cell Mol. Biol.* **326**, 343–372 (2016).
63. E. Arico, L. Castiello, I. Capone, L. Gabriele, F. Belardelli, Type I interferons and cancer: An evolving story demanding novel clinical applications. *Cancers* **11**, 1943 (2019).
64. X. Chen, M. Bäumel, D. N. Männel, O. M. Howard, J. J. Oppenheim, Interaction of TNF with TNF receptor type 2 promotes expansion and function of mouse $CD4^+CD25^+$ T regulatory cells. *J. Immunol.* **179**, 154–161 (2007).
65. T. Schioppa, R. Moore, R. G. Thompson, E. C. Rosser, H. Kulbe, S. Nedospasov, C. Mauri, L. M. Coussens, F. R. Balkwill, B regulatory cells and the tumor-promoting actions of TNF-α during squamous carcinogenesis. *Proc. Natl. Acad. Sci. U.S.A.* **108**, 10662–10667 (2011).
66. X. Zhao, L. Rong, X. Zhao, X. Li, X. Liu, J. Deng, H. Wu, X. Xu, U. Erben, P. Wu, U. Syrbe, J. Sieper, Z. Qin, TNF signaling drives myeloid-derived suppressor cell accumulation. *J. Clin. Invest.* **122**, 4094–4104 (2012).
67. D. Zink, A. H. Fischer, J. A. Nickerson, Nuclear structure in cancer cells. *Nat. Rev. Cancer* **4**, 677–687 (2004).
68. J. Todoric, L. Antonucci, M. Karin, Targeting inflammation in cancer prevention and therapy. *Cancer Prev. Res.* **9**, 895–905 (2016).
69. A. Martin-Ruiz, C. Fiuza-Luces, E. Martinez-Martinez, C. F. Arias, L. Gutierrez, M. Ramirez, P. Martin-Acosta, M. J. Coronado, A. Lucia, M. Provencio, Effects of anti-PD-1 immunotherapy on tumor regression: Insights from a patient-derived xenograft model. *Sci. Rep.* **10**, 7078 (2020).
70. J. Fricke, I. Mambetsariev, R. Pharaon, S. Subbiah, S. Rajurkar, R. Salgia, Hyperprogression on immunotherapy with complete response to chemotherapy in a NSCLC patient with high PD-L1 and STK11: A case report. *Medicine* **99**, e22323 (2020).
71. A. Forschner, F. J. Hilke, I. Bonzheim, A. Gschwind, G. Demidov, T. Amaral, S. Ossowski, O. Riess, C. Schroeder, P. Martus, B. Klumpp, I. Gonzalez-Menendez, C. Garbe, H. Niessner, T. Sinnberg, MDM2, MDM4 and EGFR amplifications and hyperprogression in metastatic acral and mucosal melanoma. *Cancers* **12**, 540 (2020).
72. Y. Khagi, R. Kurzrock, S. P. Patel, Next generation predictive biomarkers for immune checkpoint inhibition. *Cancer Metastasis Rev.* **36**, 179–190 (2017).
73. S. L. Topalian, J. M. Taube, R. A. Anders, D. M. Pardoll, Mechanism-driven biomarkers to guide immune checkpoint blockade in cancer therapy. *Nat. Rev. Cancer* **16**, 275–287 (2016).
74. F. A. Ran, P. D. Hsu, J. Wright, V. Agarwala, D. A. Scott, F. Zhang, Genome engineering using the CRISPR-Cas9 system. *Nat. Protoc.* **8**, 2281–2308 (2013).
75. Y. W. Zhang, D. M. Otterness, G. G. Chiang, W. Xie, Y. C. Liu, F. Mercurio, R. T. Abraham, Genotoxic stress targets human Chk1 for degradation by the ubiquitin-proteasome pathway. *Mol. Cell* **19**, 607–618 (2005).

Acknowledgments: We thank Y. Li (College of Pharmacy, Jinan University, China) for creating the model graph. **Funding:** R.E.C. was supported by NIGMS/NIH R01GM134531, and E.G.H was supported by T32CA009156 to the Lineberger Cancer Center. This work was supported, in part, by NCI/NIH (CA163214 and CA230453), the American Cancer Society (ACS RSG-15-042 DMC), the Clinical and Translational Science Collaborative (CTSC) of Cleveland UL1TR000439 from the NCATS/NIH, institutional VeloSano Bike to Cure Pilot grant, and a Case Comprehensive Cancer Center Pilot grant (P30CA043703) to Y.Z. **Author contributions:** F.M.P. and Y.Z. conceived the project. F.M.P. acquired most of the data and performed the analyses. X.G. contributed to the revision. I.T. and M.W.J. participated in the EMT study. E.G.H., J.A.H., and R.E.C. provided *MYO10* knockout mice and insights. F.M.P. and Y.Z. wrote the manuscript. **Competing interests:** The authors declare that they have no competing interests. **Data and materials availability:** All data needed to evaluate the conclusions in the paper are present in the paper and/or the Supplementary Materials.

Submitted 21 January 2021
Accepted 26 July 2021
Published 15 September 2021
10.1126/sciadv.abg6908

Citation: F. Mayca Pozo, X. Geng, I. Tamagno, M. W. Jackson, E. G. Heimsath, J. A. Hammer, R. E. Cheney, Y. Zhang, MYO10 drives genomic instability and inflammation in cancer. *Sci. Adv.* **7**, eabg6908 (2021).